PROPER MOTIONS OF DWARF SPHEROIDAL GALAXIES FROM *HUBBLE SPACE TELESCOPE* IMAGING. III. MEASUREMENT FOR URSA MINOR[1]

Slawomir Piatek
Department of Physics, New Jersey Institute of Technology, Newark, NJ 07102; piatek@physics.rutgers.edu

Carlton Pryor
Department of Physics and Astronomy, Rutgers, The State University of New Jersey,
136 Frelinghuysen Road, Piscataway, NJ 08854-8019; pryor@physics.rutgers.edu

Paul Bristow
Space Telescope European Coordinating Facility, Karl-Schwarzschild-Strasse 2,
D-85748 Garching bei Munchen, Germany; bristowp@eso.org

Edward W. Olszewski
Steward Observatory, University of Arizona, Tucson, AZ 85721; eolszewski@as.arizona.edu

Hugh C. Harris
US Naval Observatory, Flagstaff Station, P.O. Box 1149, Flagstaff, AZ 86002-1149; hch@nofs.navy.mil

Mario Mateo
Department of Astronomy, University of Michigan, 830 Dennison Building, Ann Arbor, MI 48109-1090; mateo@astro.lsa.umich.edu

Dante Minniti
Department of Astronomy and Astrophysics, Universidad Catolica de Chile, Casilla 306, Santiago 22, Chile; dante@astro.puc.cl

and

Christopher G. Tinney
Anglo-Australian Observatory, P.O. Box 296, Epping 1710, Australia; cgt@aaoepp.aao.gov.au

ABSTRACT

This article presents a measurement of the proper motion of the Ursa Minor dwarf spheroidal galaxy determined from images taken with the *Hubble Space Telescope* in two distinct fields. Each field contains a quasi-stellar object that serves as the "reference point." The measured proper motion for Ursa Minor, expressed in the equatorial coordinate system, is $(\mu_\alpha, \mu_\delta) = (-50 \pm 17, 22 \pm 16)$ mas century^{-1}. Removing the contributions of the solar motion and the motion of the local standard of rest yields the proper motion in the Galactic rest frame: $(\mu_\alpha^{\mathrm{Grf}}, \mu_\delta^{\mathrm{Grf}}) = (-8 \pm 17, 38 \pm 16)$ mas century^{-1}. The implied space velocity with respect to the Galactic center has a radial component of $V_r = -75 \pm 44$ km s^{-1} and a tangential component of $V_t = 144 \pm 50$ km s^{-1}. Integrating the motion of Ursa Minor in a realistic potential for the Milky Way produces orbital elements. The perigalacticon and apogalacticon are 40 (10, 76) and 89 (78, 160) kpc, respectively, where the values in the parentheses represent the 95% confidence intervals derived from Monte Carlo experiments. The eccentricity of the orbit is 0.39 (0.09, 0.79), and the orbital period is 1.5 (1.1, 2.7) Gyr. The orbit is retrograde and inclined by 124° (94°, 136°) to the Galactic plane. Ursa Minor is not a likely member of a proposed stream of galaxies on similar orbits around the Milky Way, nor is the plane of its orbit coincident with a recently proposed planar alignment of galaxies around the Milky Way. Comparing the orbits of Ursa Minor and Carina shows no reason for the different star formation histories of these two galaxies. Ursa Minor must contain dark matter to have a high probability of having survived disruption by the Galactic tidal force until the present.

Key words: astrometry — galaxies: dwarf — galaxies: individual (Ursa Minor)

1. INTRODUCTION

The Ursa Minor dwarf spheroidal galaxy (dSph), detected by Wilson (1955) on plates of the Palomar Sky Survey, is at $(\alpha, \delta) = (15^{\mathrm{h}}09^{\mathrm{m}}11^{\mathrm{s}}, 67°12'54'')$ (J2000.0; Mateo 1998) on the sky. Its Galactic coordinates are $(l, b) = (104°.95, 44°.80)$. Several published estimates of the distance to Ursa Minor disagree by more than their combined uncertainties. Olszewski & Aaronson (1985) and Cudworth et al. (1986) determine a distance modulus, $(m - M)_0$, of 19.0 ± 0.1, which corresponds to

a heliocentric distance of 63 ± 3 kpc. These two studies are not independent because they use the same photometric calibration. This distance is in agreement with those measured by Nemec et al. (1988), 70 ± 9 kpc, and Mighell & Burke (1999), 69 ± 4 kpc. The latter value comes from *V* and *I* images of the central region in Ursa Minor taken with the *Hubble Space Telescope* (*HST*). However, Carrera et al. (2002) determine $(m - M)_0 = 19.4 \pm 0.1$, which gives a distance of 76 ± 4 kpc (note an erroneous entry of 70 kpc for the distance in their Table 3). Bellazzini et al. (2002) find a similar value: $(m - M)_0 = 19.41 \pm 0.12$. About 0.3 mag of the 0.41 mag difference between the distance moduli of Cudworth et al. (1986) and Bellazzini et al. (2002) comes from different values for the absolute magnitude of the horizontal branch. It is beyond
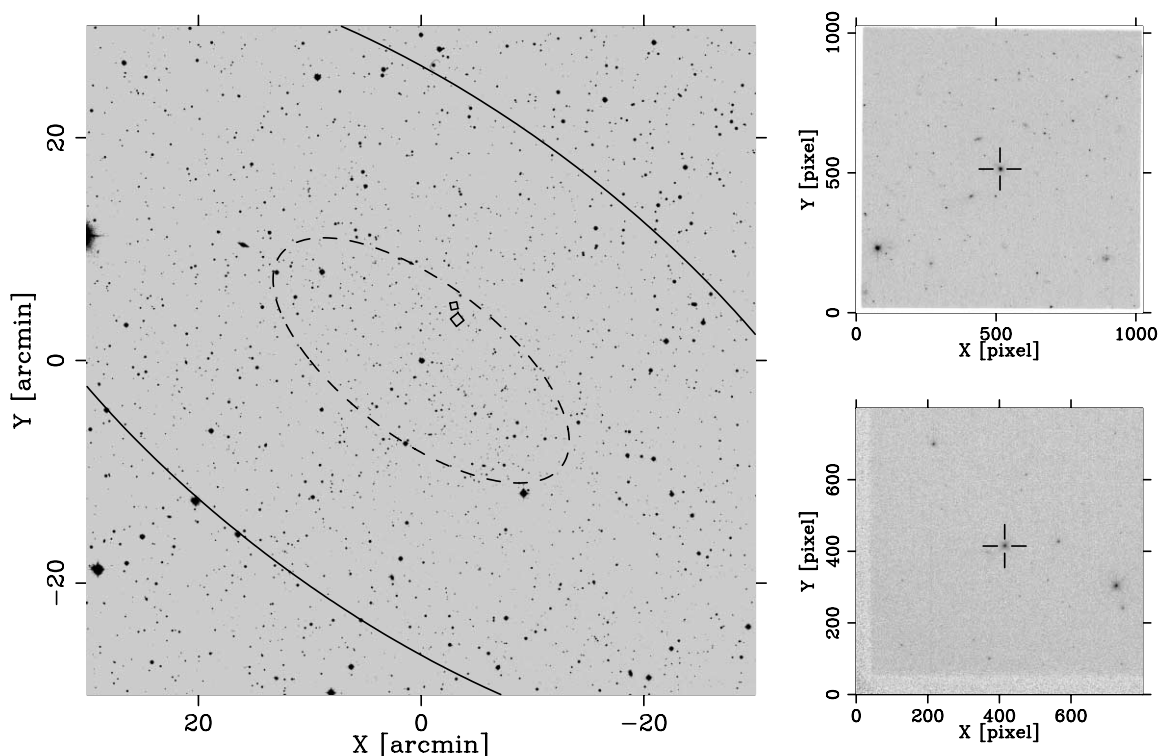
Fig. 1.—*Left*: Image of the sky in the direction of the Ursa Minor dSph. The dashed ellipse is the measured core radius, and the solid ellipse is the measured tidal boundary. The two squares represent the fields studied in this article. The larger of the two corresponds to the UMI J1508+6716 field, and the smaller to the UMI J1508+6717 field. *Top right*: Sample image from the epoch 2000 data for the UMI J1508+6716 field. The cross-hair indicates the location of the QSO. *Bottom right*: Sample image from the epoch 1999 data for the UMI J1508+6717 field. Again, the cross-hair indicates the location of the QSO.

the scope of this article to resolve the uncertainties in the globular cluster distance scale; however, the larger distance is based on more modern stellar models and is probably in better agreement with *Hipparcos* parallaxes for subdwarfs (Reid 1997; Gratton et al. 1997) and the age of the universe derived by the *Wilkinson Microwave Anisotropy Probe* (*WMAP*; Bennett et al. 2003). Thus, this study adopts a distance of 76 kpc for the purpose of deriving distance-dependent quantities.

Ursa Minor is one of the least luminous Galactic dSphs. Irwin & Hatzidimitriou (1995, hereafter IH95) report its luminosity to be $L_V = (2.0 \pm 0.9) \times 10^5 \, L_\odot$. Reflecting their larger estimate of the distance, Carrera et al. (2002) report $L_V = 3 \times 10^5 \, L_\odot$. These luminosities are based on the structural parameters from IH95: a core radius of $15'.8 \pm 1'.2$ and a tidal radius of $50'.6 \pm 3'.6$. Kleyna et al. (1998) find similar structural parameters for Ursa Minor. However, Martínez-Delgado et al. (2001) and Palma et al. (2003) find a more extended radial profile, which implies a larger luminosity. Palma et al. (2003) determine that both blue horizontal branch stars and stars identified as giants on the basis of photometry in the Washington-band system extend beyond the tidal radius of IH95. They argue that the luminosity of Ursa Minor is 2.7 times larger than the value of IH95. Based on both the larger radial extent and the larger distance, Bellazzini et al. (2002) adopt a luminosity of $(1.1 \pm 0.4) \times 10^6 \, L_\odot$. Our study likewise adopts this value.

Several studies find that the stars of Ursa Minor are old, metal-poor, and of similar age. Olszewski & Aaronson (1985) constructed a V versus $B - V$ color-magnitude diagram for the dSph using data from ground-based observations. The diagram reveals that the stars of Ursa Minor have ages and metallicities similar to those of the metal-poor globular cluster M92. The study interprets the few stars brighter and bluer than the main-

sequence turnoff as blue stragglers. Carrera et al. (2002) confirm this basic picture using ground-based data in the B, V, R, and I bands. An analysis of *HST* data by Mighell & Burke (1999) reveals the same picture: the stars of Ursa Minor are about 14 Gyr old, formed in a single burst that lasted less than 2 Gyr, and are metal-poor, with a metallicity $[\mathrm{Fe/H}] \approx -2.2$ dex. All of these characteristics indicate that the stars in Ursa Minor formed in a single burst during the earliest stages of the formation of our Galaxy. Ursa Minor has little or no gas: searches for neutral hydrogen by Young (2000) and for ionized hydrogen by Gallagher et al. (2003) yield no positive detections, only placing upper limits of $7 \times 10^3 \, M_\odot$ on H I and $1 \times 10^5 \, M_\odot$ on H II. The absence of gas is consistent with the old stellar population in Ursa Minor; however, the question of why Ursa Minor quickly stopped forming stars whereas the similar dSph Carina did not remains unanswered.

With the possible exception of Sagittarius, Ursa Minor has the greatest flattening among the known Galactic dSphs. IH95 derive an ellipticity of 0.56 ± 0.05 and a position angle for the major axis of $53° \pm 5°$. Kleyna et al. (1998) derive similar values. The ellipticity of Ursa Minor is distinctly larger than those of the other dSphs (again excluding Sagittarius), which range from 0.1 to 0.35 (IH95). Figure 1 (*left*) shows a $1° \times 1°$ section of the sky in the direction of Ursa Minor from the Digitized Sky Survey. The dashed and solid ellipses delineate the core and tidal radii of Ursa Minor from IH95.

Hartwick & Sargent (1978) and Aaronson (1983) were the first to measure radial velocities for one to two stars in Ursa Minor, finding a systemic velocity of about -250 km s^{-1}. Hargreaves et al. (1994) find a mean heliocentric radial velocity of -249.2 ± 1.5 km s^{-1} from the radial velocities of 35 giants. Armandroff et al. (1995) combined the data from Hargreaves

et al. (1994) and from Olszewski et al. (1995) with their own measurements to obtain mean radial velocities for a sample of 94 stars. Excluding one possible nonmember, the mean heliocentric radial velocity is -247.4 ± 1.0 km s^{-1}. Our study adopts this last value. The adopted value is in reasonable agreement with the most recent determination of this quantity by Wilkinson et al. (2004), who derive $-245.2^{+1.0}_{-0.6}$ km s^{-1} from the measured radial velocities for 162 stars.

The dispersion of velocities within a dSph provides information about its mass and how the mass is distributed. Aaronson & Olszewski (1987) report a velocity dispersion for Ursa Minor of 11 ± 3 km s^{-1} from the radial velocities of seven stars. This dispersion indicated for the first time that the mass greatly exceeds that expected from stars alone. Subsequent measurements have confirmed the large dispersion; Hargreaves et al. (1994) find $7.5^{+1.0}_{-0.9}$ km s^{-1} from a sample of 35 giants, and Armandroff et al. (1995) find 8.8 ± 0.8 km s^{-1} from a sample of 93 giants. The larger sample of radial velocities in Wilkinson et al. (2004) provides information on the dependence of velocity dispersion on the projected radius. The bottom panel of their Figure 1 shows that the velocity dispersion is constant at about 12 km s^{-1} to a radius of approximately $32'$; beyond this radius, the velocity dispersion drops sharply to about 2 km s^{-1}. Hargreaves et al. (1994) and Armandroff et al. (1995) assume virial equilibrium, that light follows mass, and the luminosity and structural parameters from IH95 to calculate a mass-to-light ratio in solar units, M/L_V, of 50^{+36}_{-22} and 55 ± 10, respectively. The uncertainty for the second of these values includes only the contribution from the velocity dispersion, whereas the uncertainty for the first value includes the contributions from all the relevant parameters. Making the same assumptions and using one of the above velocity dispersions, IH95, Kleyna et al. (1998), and Carrera et al. (2002) infer similarly large values of M/L_V: 95 ± 43, 70^{+30}_{-20}, and 70, respectively.

In contrast, Palma et al. (2003) find $M/L_V = 47$. They derive a surface density profile from a sample of stars selected to be members of Ursa Minor using three-color Washington-band photometry. Fitting a King model to this profile produces a tidal radius of $77\rlap{.}'9 \pm 8\rlap{.}'9$. This value is larger than those derived by IH95 and Kleyna et al. (1998), which affects the derived mass and luminosity of the galaxy. Palma et al. (2003) also note that the M/L could be even smaller if the velocity dispersion tensor of the dSph were anisotropic. Richstone & Tremaine (1986) caution that the M/L calculated using King's method will be overestimated or underestimated depending on whether the velocity dispersion is larger in the radial or tangential directions, respectively. Despite a lack of any evidence for an anisotropic dispersion tensor, Palma et al. (2003) conclude that the M/L_V of Ursa Minor may be as low as 16. The larger distance, and hence larger luminosity, found by Bellazzini et al. (2002) further reduces the lower limit on the M/L_V to 7.

Palma et al. (2003) note that a power law with an index of -3 is a better fit to the surface density profile of Ursa Minor at radii between $20'$ and $100'$ than is a King model. They argue that such a profile indicates that the Galactic tidal force has produced a halo of escaping stars around the dSph. They also argue that a M/L near the lower limit allowed by the uncertainty in the mass estimate is more consistent with a picture in which "this system is very likely undergoing significant mass loss due to its tidal interaction with the Milky Way."

Gómez-Flechoso & Martínez-Delgado (2003) have made the above argument more quantitative. They derive $M/L_V = 12$ for Ursa Minor by evolving an N-body model of the dSph in a potential of the Milky Way on an orbit constrained by the proper motion of the dSph from Schweitzer et al. (1997), varying the M/L of the dSph in order to match the surface brightness profile of the model dSph with the observed profile. The study finds that an acceptable match exists only if Ursa Minor has M/L_V within a factor of 2 of 12. Gómez-Flechoso & Martínez-Delgado (2003) argue that their lower value for the M/L is consistent with the values derived from the velocity dispersion if the maximum possible effect from radial anisotropy is taken into account. They also argue that the observed velocity dispersion "could be inflated by the effects of the substructures in the main body" or by departures from virial equilibrium due to the Galactic tidal force.

The numerical simulations of Piatek & Pryor (1995) show that, if the Galactic tidal force causes a departure from virial equilibrium, then escaping stars produce a velocity gradient—an apparent rotation—along the projected major axis of the dSph. Hargreaves et al. (1994) and Armandroff et al. (1995) both found a statistically significant velocity gradient but along the minor axis instead of the major axis. Subtracting the velocity gradient from the radial velocities does not reduce the measured velocity dispersion significantly. Kroupa (1997) and Klessen & Kroupa (1998) show that the velocity gradient is hidden if the tidal debris is aligned along the line of sight to the dSph. Palma et al. (2003) rule out this alignment because it would produce more broadening of the horizontal branch than they observe. Thus, a departure from virial equilibrium cannot explain the difference between the M/L found by Gómez-Flechoso & Martínez-Delgado (2003) and those found using the measured velocity dispersion.

Olszewski & Aaronson (1985) discovered a statistically significant change in surface density across their $3' \times 5'$ field and interpreted this variation as evidence for substructure in Ursa Minor. It is now known that the highest peak in the surface density of the dSph is near the eastern edge of this field. Demers et al. (1995) also detect a statistically significant clump of stars at the same location, which causes a step in the surface density profile at a radius of about $1'$. The deep HST photometry of Battinelli & Demers (1999) supports the existence of this clump and may also suggest the presence of additional structure within the clump. Other studies of substructure have focused on a possible secondary peak or "shoulder" in the surface density profile, first noted by IH95, that is about $15'$ northeast of the primary peak. Kleyna et al. (1998), Eskridge & Schweitzer (2001), and Palma et al. (2003) demonstrate that a "shoulder" in the profile is statistically significant, although a secondary peak is not. Kleyna et al. (2003) used measured radial velocities for stars in Ursa Minor to demonstrate the presence of a distinct subpopulation with a velocity dispersion of 0.5 km s^{-1}—much smaller than the 8.8 km s^{-1} of the whole sample of velocities—at the location of the "shoulder." Excluding the stars in this substructure from the sample would increase the measured velocity dispersion of the dSph and thus the inferred M/L. Thus, the presence of substructure does not reconcile the M/L found by Gómez-Flechoso & Martínez-Delgado (2003) with that derived from the velocity dispersion.

Two pictures of Ursa Minor emerge from the above discussion. (1) Dark matter is the main component of the mass of Ursa Minor, and therefore, it determines the structure and internal dynamics of the dSph. (2) Ursa Minor contains little or no dark matter, and therefore, the Galactic tidal force has had and continues to have an important effect on the structure and internal dynamics of the dSph. Knowing the proper motion of Ursa Minor can help to discriminate between these two pictures by constraining the orbit and thus the strength of the

Galactic tidal force on Ursa Minor. If the perigalacticon is small, Ursa Minor would need to contain a large amount of dark matter to have survived until now. The presence of tidal signatures need not indicate that the dSph is out of virial equilibrium or that it contains only luminous matter. Conversely, a large perigalacticon would require a low M/L for the dSph so that the Galactic tidal force could have produced the observed signatures.

A proper motion for Ursa Minor also tests the hypothesis that it is a member of a "stream" of objects in the Galactic halo that share a similar orbit. Lynden-Bell & Lynden-Bell (1995) propose that Ursa Minor, the Large Magellanic Cloud (LMC), the Small Magellanic Cloud (SMC), and the Draco and possibly also Sculptor and Carina galaxies form a stream. They propose that such a stream forms from the fragments of a larger, tidally disrupted galaxy. The theory of streams in the Galactic halo is falsifiable because it predicts a proper motion for each member of the stream. There is some controversy regarding the reality of this stream: Anguita et al. (2000) measured the proper motion of the LMC and found that it is inconsistent with the prediction of Lynden-Bell & Lynden-Bell (1995), whereas the proper motions measured by Jones et al. (1994) and Kroupa & Bastian (1997) are consistent.

There are two independent published results for the proper motion of Ursa Minor. Scholz & Irwin (1993) used Palomar Sky Survey plates for the first and second epochs, which are separated by about 26 yr, and plates taken with the Tautenburg Schmidt telescope for the third epoch, which provides a total time baseline of about 31 yr. They find a proper motion, "as is on the sky," of $(50 \pm 80, 120 \pm 80)$ mas century^{-1} (the last row in their Table 3, but using an uncertainty 80 instead of 20 mas century^{-1} for μ_δ, as implied by the text). Schweitzer (1996) and Schweitzer et al. (1997) used a total of 39 photographic plates taken with the Palomar 5 m Hale telescope (first epoch) and the Kitt Peak National Observatory 4 m telescope (second and third epochs). The time between the first- and third-epoch images is about 42 yr. Schweitzer (1996) reports a proper motion of $(5.6 \pm 7.8, 7.4 \pm 9.9)$ mas century^{-1}. The proper motions measured by these two studies agree within their uncertainties.

Here we present a third independent measurement of the proper motion of Ursa Minor. The measurement derives from images of two distinct fields, each containing a known quasi-stellar object (QSO), taken with *HST*. Sections 2, 3, and 4 describe the data, the derivation of mean centroids at each epoch, and the derivation of the proper motion from the centroids, respectively. The last of these sections contains a comparison of our measured proper motion with those determined by Scholz & Irwin (1993) and Schweitzer (1996; see also Schweitzer et al. 1997). Section 5 derives orbital elements in a realistic potential for the Milky Way. Section 6 discusses the implications of the orbit of Ursa Minor for (1) its membership in proposed structures in the Galactic halo, (2) its star formation history, (3) the mass of the Milky Way, and (4) the importance of the Galactic tidal force and thus whether the dSph contains dark matter. Finally, § 7 summarizes our main results.

2. OBSERVATIONS AND DATA

The data comprise images of two distinct fields in the direction of Ursa Minor taken at three epochs with *HST*. A known QSO is at, or close to, the center of each field. Figure 1 (*left*) shows the locations of the two fields on the sky. Both fields are within the core radius and close to the minor axis. *HST* imaged the larger of the two fields, UMI J1508+6716, on 2000 February 16, 2001 February 15, and 2002 February 1, using the
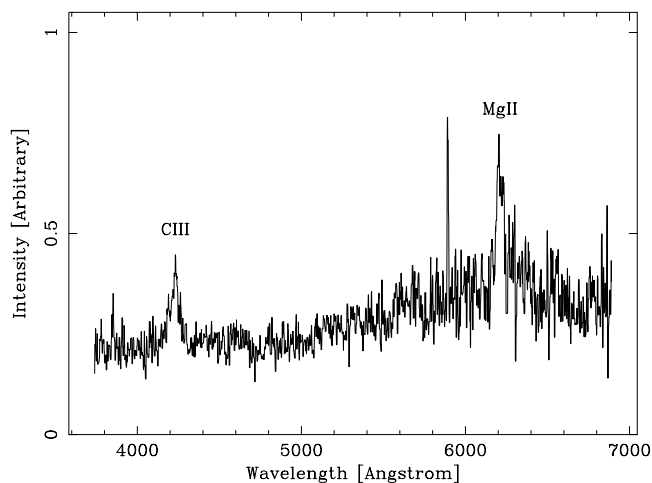

Fig. 2.—Spectrum of the QSO in the UMI J1508+6716 field taken with the Blue Channel Spectrograph and the 500 line grating on the MMT on 2004 January 19. This setup gives a resolution of 3.6 Å and a coverage of 3200 Å. The spectrum is the sum of two 600 s exposures, and it has been smoothed by a running median of five points. The measured redshift is 1.216.

Space Telescope Imaging Spectrograph (STIS) with no filter (50CCD). Ursa Minor was in the continuous viewing zone during the first two epochs and was not during the last. Each of the eight dither positions has six images at the first two epochs, for a total of 48 images per epoch, while each dither position has only three, for a total of 24 images, at the last epoch. The average exposure times for the three epochs are 176, 176, and 210 s, respectively. The QSO in this field is at $(\alpha, \delta) = (15^h08^m37\overset{s}{.}661, +67°16'34\overset{''}{.}27)$ (J2000.0). From Bellazzini et al. (2002), its *V*- and *I*-band magnitudes are 20.3 and 19.7, respectively. Figure 2 shows a spectrum of the QSO, which indicates a redshift of 1.216. Figure 1 (*top right*) shows a sample image of this field from the 2000 epoch. The image is the average of six images at one dither position with cosmic rays removed. The cross-hair indicates the location of the QSO.

HST imaged the smaller of the two fields, UMI J1508+6717, on 1999 March 14, 2001 March 10, and 2003 March 2 using the Planetary Camera (PC) of the Wide Field Planetary Camera 2 (WFPC2) and the F606W filter. There are 40 images for the first epoch, 36 for the second, and 36 for the third. The exposure time is 160 s for each image. Here the QSO is at $(\alpha, \delta) = (15^h08^m40\overset{s}{.}410, +67°17'47\overset{''}{.}50)$ (J2000.0), its *V*- and *I*-band magnitudes are 19.7 and 18.9, respectively (Bellazzini et al. 2002), and Figure 3 shows its spectrum. The spectrum implies a redshift of 0.716. Figure 1 (*bottom right*) depicts an average of three images in this field from the 1999 epoch, with cosmic rays removed. The cross-hair indicates the location of the QSO. Note the scarcity of stars in both sample images.

Bristow (2004) notes that the decreasing charge transfer efficiency in the STIS and WFPC2 CCDs may induce a spurious contribution to the proper motion measured with the method described by Piatek et al. (2002, 2003, hereafter P02, P03). The cosmic particle radiation damages the crystal lattice of a detector, creating "charge traps," and the number of these traps increases with time. During the readout, charge moves along the *Y*-axis: "up," or toward the increasing *Y*-values, for STIS and "down," or in the direction of decreasing *Y*-values, for PC. Charge moves "left," toward decreasing *X*-values in the serial register. When a "packet" of charge corresponding to some object encounters a trap, it loses some of its charge. A passing packet partially fills a trap, so a subsequent packet loses less
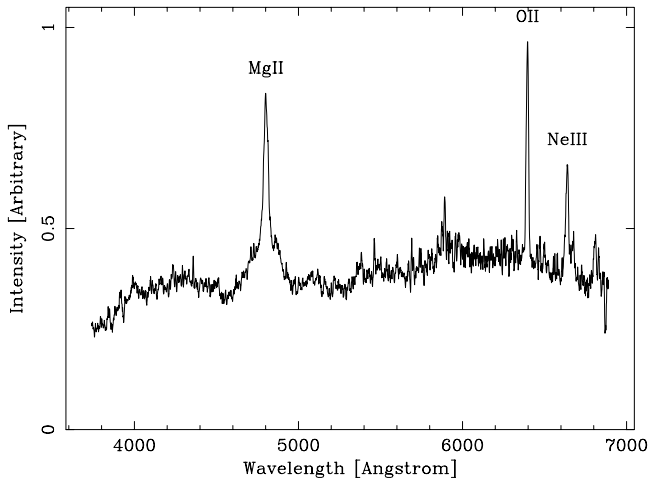
Fig. 3.—Same as Fig. 2 but for the QSO in the UMI J1508+6717 field. This single 600 s exposure has been smoothed with a running median of five points. The measured redshift is 0.716.

charge. Streaks of light along the X- and Y-axes seen trailing behind objects in the images are the visual artifacts caused by the gradual release of charge from the traps. The loss of charge for motion in the X-direction is smaller than for that in the Y-direction; it is negligible for STIS (Brown et al. 2002) and one-third as large for WFPC2 (Heyer et al. 2004). The subsequent discussion focuses only on the effect in the Y-direction.

The loss of charge to traps causes both the flux and the point-spread function (PSF) of an object to depend on its Y-coordinate in the image. The farther a packet travels, the more charge it loses. Hence, the measured flux of an object far from the serial register is smaller than that for an identical object closer to the serial register; in other words, the measured flux becomes position dependent. This effect is immaterial to our method. However, as the packets representing an object move along the Y-axis, those on its leading side partially fill each trap encountered, so that there are fewer traps available to remove charge from subsequent packets. This nonuniform loss of charge across the object changes its PSF. Consequently, the centroid of the object shifts in the direction opposite to the readout direction. The shift is greatest for objects that are farthest from the serial register. It is also larger for faint objects than for bright objects (Bristow & Alexov 2002). This effect changes the measured proper motion only because the number of charge traps increases with time, thus causing the shift of a centroid to also change with time. The analysis of Bristow (2004) warns that this spurious proper motion may be comparable to the actual proper motion of a dSph.

There are two possible approaches to removing the effect of the spurious shifts of the centroids along the Y-axis with time. In the first approach, the images are corrected by restoring the trapped charge to its original packet. This correction requires that the distribution and the properties of the charge traps be known. Bristow & Alexov (2002) constructed a physical model of the charge traps and then wrote a computer code that makes the aforementioned correction for an image taken with STIS. Unless stated otherwise, the results presented are for corrected images. No comparable software exists for WFPC2, unfortunately. A second approach to correcting for the decreasing charge transfer efficiency is including a term that varies linearly with Y in the equations that transform the coordinates of an object at different epochs to a common coordinate system. The coefficients of these transformations are fitted as described in

§ 4.1. The analysis of the data taken with WFPC2 uses this approach.

3. ANALYSIS OF DATA

The analysis of the data and derivation of the proper motion of Ursa Minor are basically the same as described in P02. P03 provides some additional insight into the method. This article only lists the principal steps here and comments, where appropriate, on several changes in the details of the analysis. The principal steps of the analysis are as follows: (1) Using the DAOPHOT and ALLSTAR software packages (Stetson 1987, 1992, 1994), determine an initial estimate of the centroid of each object: stars and the QSO. (2) Construct an effective point-spread function (ePSF; Anderson & King 2000) for each epoch separately from a select set of stars and the QSO. (3) Iteratively fit the ePSF to an image of an object using least-squares to derive a more accurate centroid of the object and, using these more accurate centroids, derive a more accurate ePSF. Repeat until a stable solution ensues. There may be a maximum of N centroids for an object, where N is the number of images. (4) Transform the centroids measured at one epoch to a common (fiducial) coordinate system and calculate the average. The fiducial coordinate system for an epoch is the X-Y coordinate system of the chronologically first image. (5) Determine the transformation between the fiducial coordinate systems of the later epochs and that of the first epoch using stars that are likely members of Ursa Minor and common to all three epochs. The fit for the transformation simultaneously determines the change with time of the coordinates of some objects, μ_x and μ_y in pixels yr^{-1}. Ideally, these objects are not members of Ursa Minor. The set of objects whose motion is fitted is built starting with the QSO and iteratively adding one object at a time, in order of descending χ^2 for the scatter about the mean coordinate, until the highest χ^2 of an object not yet in the set is below a specified limit. The shifts are with respect to stars of Ursa Minor that by definition have $\mu_x = \mu_y = 0$. This procedure for deriving the values of μ_x and μ_y for objects is new to our method; § 4 below discusses its details. The advantage of this new method over that used by P02 and P03 is that it more accurately includes the contribution from the uncertainty in the coordinate transformation between epochs to the uncertainty in the proper motion. (6) Derive the proper motion of Ursa Minor from the μ_x and μ_y of the QSO.

Before calculating the transformation to the fiducial coordinate system, the centroids measured in each image taken with WFPC2 are corrected for the 34th row defect (Shaklan et al. 1995; Anderson & King 1999). In addition, all centroids are corrected for the known optical distortions in the WFPC2 and STIS instruments. This paper uses the most recent corrections for WFPC2 derived by Anderson & King (2003). The corrections for STIS continue to be those in the STIS Data Handbook (Brown et al. 2002). The following subsections present and discuss the key diagnostics of the performance of our method.

3.1. Flux Residuals

Equation (22) in P02 defines a flux residual diagnostic, $\mathcal{RF}$, which is a quantitative measure of how the shape of an object matches the ePSF. Ignoring random noise, for a perfect match, $\mathcal{RF} = 0$; otherwise, $\mathcal{RF} \neq 0$, where the sign depends on the details of the mismatch and the size of the mismatch increases with the brightness of the star. A plot of $\mathcal{RF}$ as a function of location can help unravel the dependence of the true PSF on location in an image. Our method uses a single, location-independent ePSF for deriving centroids of objects in all images for a given

field and epoch. If the true PSF of an object varies from image to image, then the $\mathcal{RF}$ values for this object will show a scatter, for example around $\mathcal{RF} = 0$ if the ePSF represents some average of the true PSFs. The plot of $\mathcal{RF}$ as a function of location will show trends if the true PSF varies with location in the image.

Figure 4 shows plots of $\mathcal{RF}$ as a function of location for the UMI J1508+6716 field. The left panels show plots of $\mathcal{RF}$ versus X, and the right panels show plots of $\mathcal{RF}$ versus Y. From top to bottom, the rows of plots are for epochs 2000, 2001, and 2002. Each plot combines points from all images for a given epoch. The filled squares mark the points corresponding to the QSO. In all six panels, the values of $\mathcal{RF}$ for the QSO are negative and distinct from those for the other objects: stars. Figure 4e and, to a lesser extent, Figure 4c show a linear trend between $\mathcal{RF}$ and X. $\mathcal{RF}$ tends to be positive around $X \approx 0$ pixels and negative around $X \approx 1000$ pixels. No other panels show a trend of $\mathcal{RF}$ with X or Y.

Figure 4 implies the following: (1) The PSF of the QSO has a different shape from that of a star. The $\mathcal{RF}$ values for the QSO become comparable to those for the stars when the value of the central pixel in the 5×5 science data array for the QSO (see P02 for a description of the structure of the data) is arbitrarily reduced by about 20%. Thus, the PSF of the QSO is narrower than that of the stars, perhaps because the QSO is bluer than the stars. (2) The PSF at a given location in the field varies from image to image, i.e., with time. This variation causes the scatter in the $\mathcal{RF}$ values of a given object. (3) The PSF varies across the field for epoch 2002 and, to a lesser degree, for epoch 2001 because the plots for those epochs show trends with location.

Figure 5 is analogous to Figure 4 for the UMI J1508+6717 field. From the top row to the bottom, the plots correspond to epochs 1999, 2001, and 2003, respectively. All the plots show that the $\mathcal{RF}$ values for the QSO are negative, with most of the points outside the plot for epoch 2001. The mean $\mathcal{RF}$ of the QSO at any epoch is more negative than the mean for any other object. For example, the object at $(X, Y) \approx (720, 300)$ is a star as bright as the QSO, but its $\mathcal{RF}$ values tend to be less negative or even positive. Again, the likely reason for the distinctness of the QSO is its narrower PSF. No plot shows an evident trend of $\mathcal{RF}$ with X or Y; however, the small number of objects contributing to these plots makes this conclusion uncertain.

3.2. Position Residuals

Figures 6 and 7 plot the position residual, $\mathcal{RX}$ or $\mathcal{RY}$, of a centroid as a function of its location within a pixel: pixel phase Φ_x or Φ_y. The position residuals are $\mathcal{RX} \equiv \langle X_0 \rangle - X_0$ and $\mathcal{RY} \equiv \langle Y_0 \rangle - Y_0$, where $\langle X_0 \rangle$ and $\langle Y_0 \rangle$ are the components of the mean centroid in the fiducial coordinate system: the system of the first image in time at a given epoch. The pixel phases are $\Phi_x \equiv X_0 - \mathrm{Int}(X_0)$ and $\Phi_y \equiv Y_0 - \mathrm{Int}(Y_0)$, where the function $\mathrm{Int}(x)$ returns the integer part of a variable x. In the presence of only random noise, the points in Figures 6 and 7 would scatter symmetrically around zero and would not exhibit any trends.

Figures 6a, 6b, and 6c plot, from top to bottom, $\mathcal{RX}$ versus Φ_x, $\mathcal{RY}$ versus Φ_y, $\mathcal{RX}$ versus Φ_y, and $\mathcal{RY}$ versus Φ_x. The panels are for the UMI J1508+6716 field, epochs 2000, 2001, and 2002, respectively. No plot in any of the panels in Figure 6 shows a trend of position residual with pixel phase.

Figure 7 is analogous to Figure 6 for the UMI J1508+6717 field. Figures 7a, 7b, and 7c correspond to epochs 1999, 2001, and 2003, respectively. No plot in Figure 7 shows a trend of position residual with pixel phase.

The figures show that the values of $\mathcal{RX}$ and $\mathcal{RY}$ for the QSO are indistinguishable from those for the stars. The smaller scatter of the values for the QSO reflects its status as one of the

brightest objects in the field. The similar distributions of the points for the QSO and the stars imply that the narrower PSF of the QSO, compared to that for the stars, does not affect the accuracy of its measured centroid.

3.3. Systematic Error in the Centroid of an Object

Kuijken & Rich (2002) show that the precision of a centroid determined by PSF fitting is proportional to $(S/N)^{-1}$ times the FWHM of the PSF. The constant of proportionality is approximately 0.67. If there is no source of error other than the uncertainty in the intensity registered by the pixel, then a plot for the entire sample of the rms scatter of the measured centroids for an object around their mean as a function of the $(S/N)^{-1}$ of the object should consist of points falling on a straight line passing through the origin. If the points fall above this straight line at large S/N, they indicate the presence of additive uncertainty, either random or systematic, that is independent of the signal. The distribution of points above and below the line is affected by the sampling uncertainty in the rms and variations in the FWHM of the PSF. The PSF can vary with location in the field, from image to image, and thus with time, or both.

Figure 8a is a plot of the rms of the X-component of a centroid (top) and of the Y-component (bottom) as a function of $(S/N)^{-1}$ for the epoch 2000 UMI J1508+6716 field. Figures 8b and 8c are the same for epochs 2001 and 2002, respectively. Note that the figures have different horizontal and vertical scales. The solid line in each plot is the best-fitting function of the form

$$\sigma = \left\{ \left[a(S/N)^{-1} \right]^2 + \sigma_0^2 \right\}^{1/2}, \qquad (1)$$

where σ is the rms scatter in either the X- or Y-direction and a and σ_0 are free parameters. Table 1 gives the fitted values of a and σ_0. Each point has equal weight in the fit. In all the plots, the adopted functional form is a good fit to the points, and the best fit requires a nonzero σ_0. The fitted slopes are in approximate agreement with the value expected for the 1.5 pixel FWHM of our ePSF. The points corresponding to the QSO are not farther from the fitted line than those corresponding to bright stars, which argues that the difference between the PSF of the QSO and of a star does not affect the rms scatter of the measured centroid of the QSO.

Figures 9a, 9b, and 9c are the corresponding plots of rms versus $(S/N)^{-1}$ for the UMI J1508+6717 field epochs 1999, 2001, and 2003, respectively. Note that the figures have different horizontal and vertical scales. The solid lines show that equation (1) is again a good fit to the points. Table 1 contains the best-fitting a and σ_0 for all three epochs. The figures and best-fitting values are similar to those for the other field.

The additive uncertainty σ_0 inferred from the fits shown in Figures 8 and 9 significantly increases the uncertainty of the final average centroid for objects with high S/N. P02 note that the rms scatter of measured centroids about their mean is smaller for measurements at a single dither position than for those at multiple dither positions. The interpretation of this was that the errors producing the additive uncertainty depend primarily on pixel phase, which argues that they arise from errors in the shape of the ePSF. Thus, the measurements of the centroid at a single dither position are not independent when the S/N is high. Both P02 and P03 calculate the larger uncertainty in the mean centroid resulting from the smaller number of independent measurements by assuming that, when the rms of a component of the centroid approaches the corresponding σ_0, the uncertainty in the average centroid approaches the rms divided by the square root of the number of
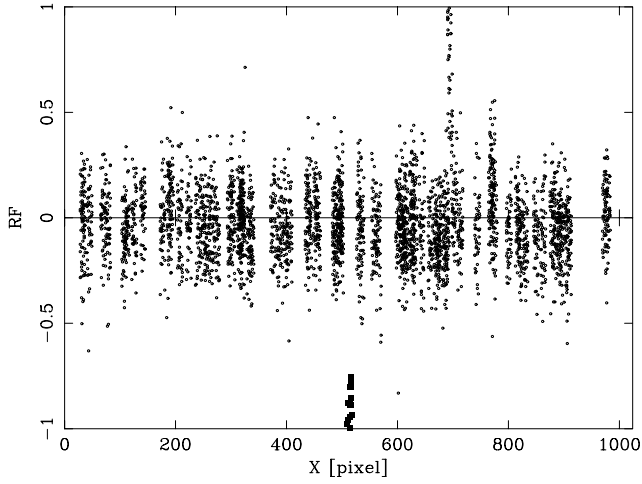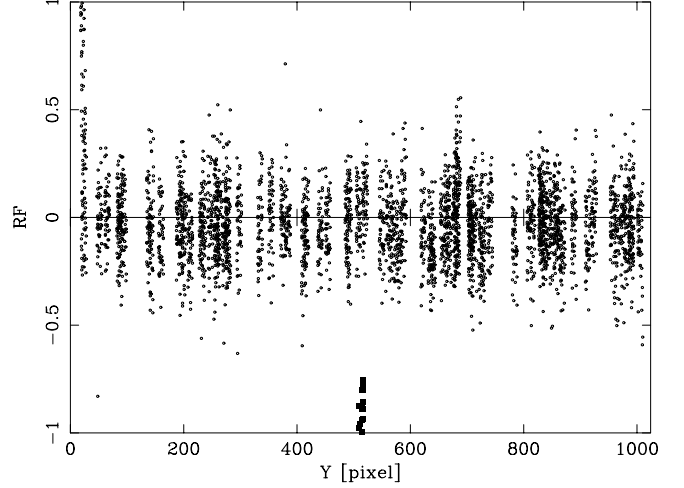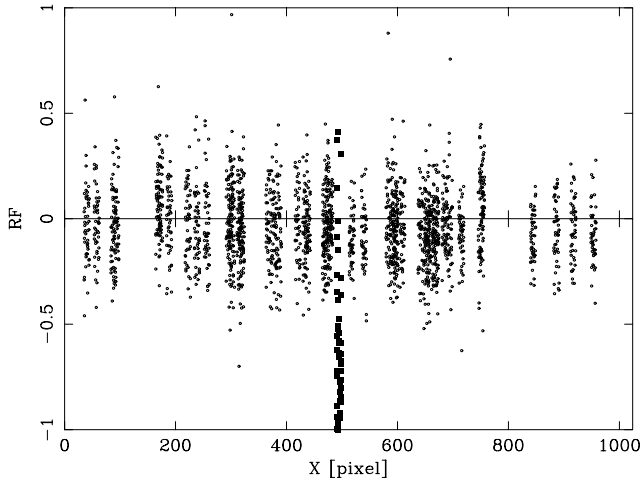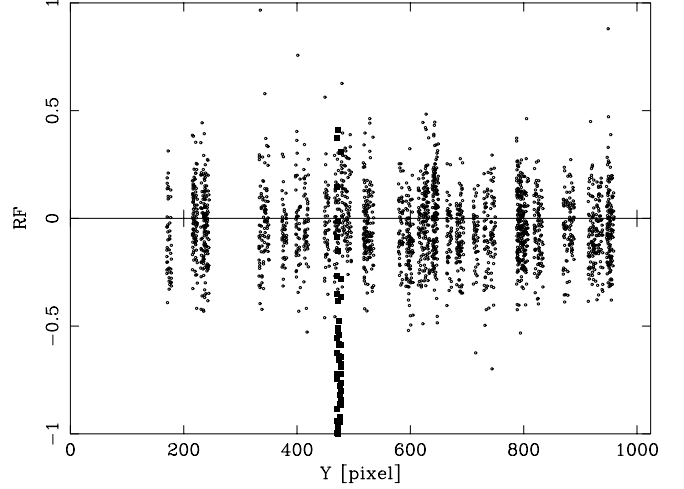
FIG. 4a
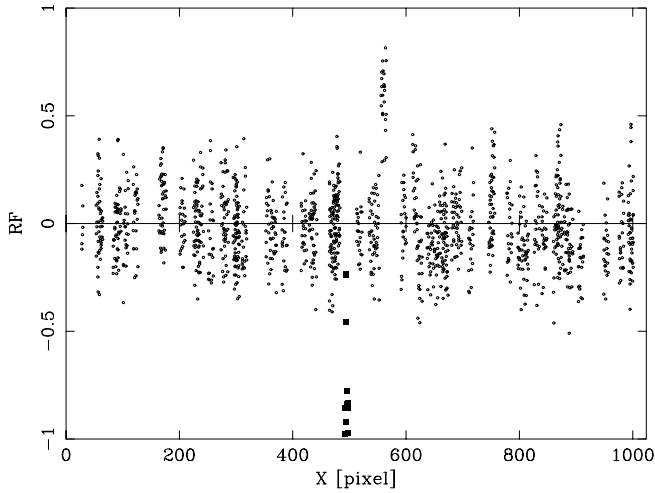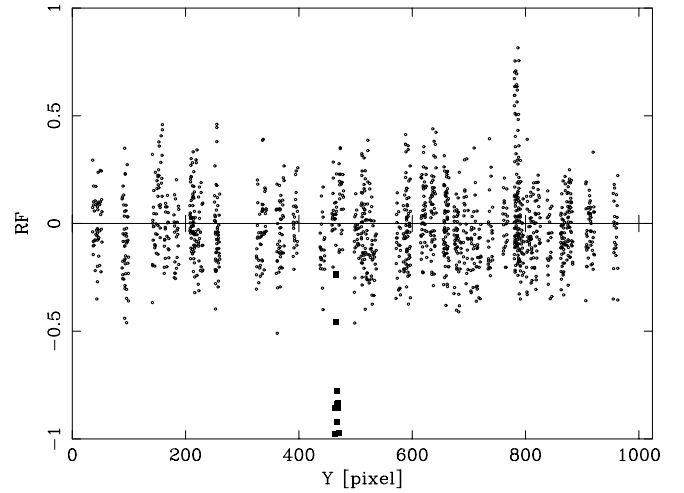
FIG. 4b

FIG. 4c

FIG. 4d

FIG. 4e

FIG. 4f

FIG. 4.—Flux residual vs. location for objects in an image for the UMI J1508+6716 field. The plots in the top two rows display points from 48 images, and the plots in the remaining row display points from 24 images. The left panels plot $\mathcal{RF}$ vs. the X-coordinate, and the right panels plot $\mathcal{RF}$ vs. the Y-coordinate. The filled squares represent the QSO. Panels a and b correspond to the 2000 epoch, c and d to the 2001 epoch, and e and f to the 2002 epoch. For ease of comparison, all the plots have the same scale on the vertical axis.
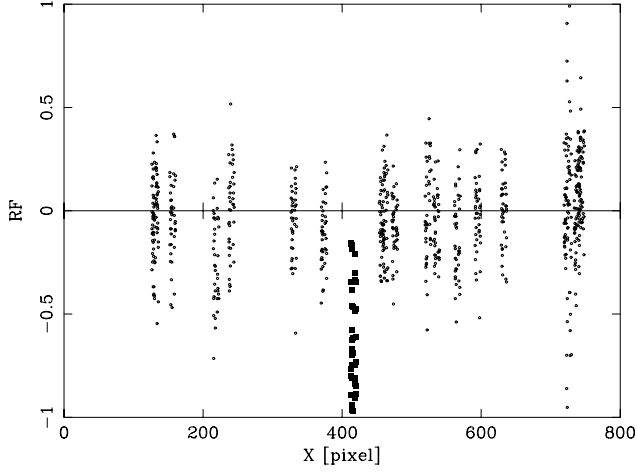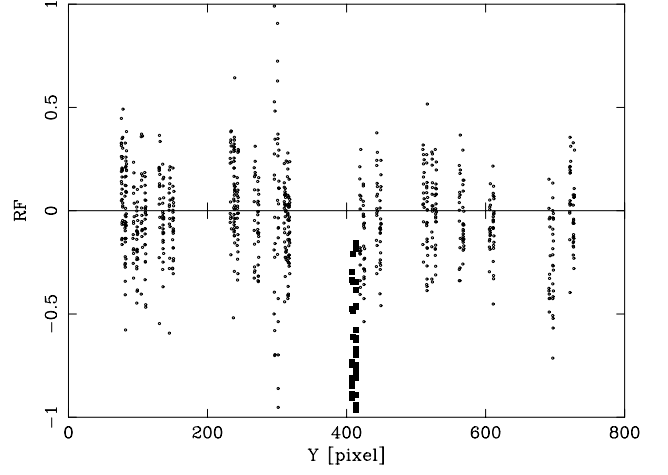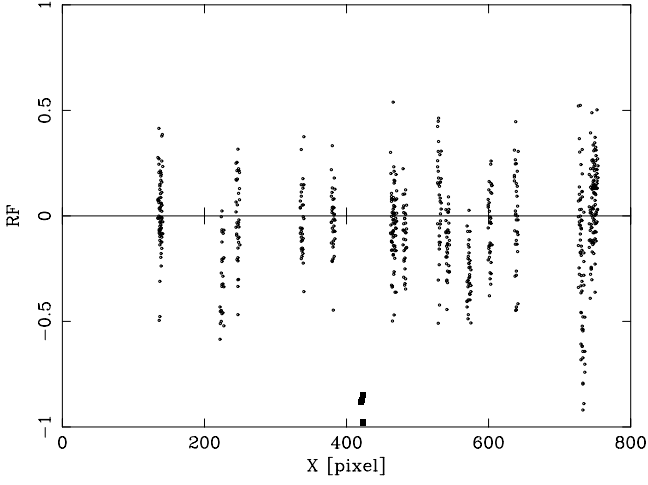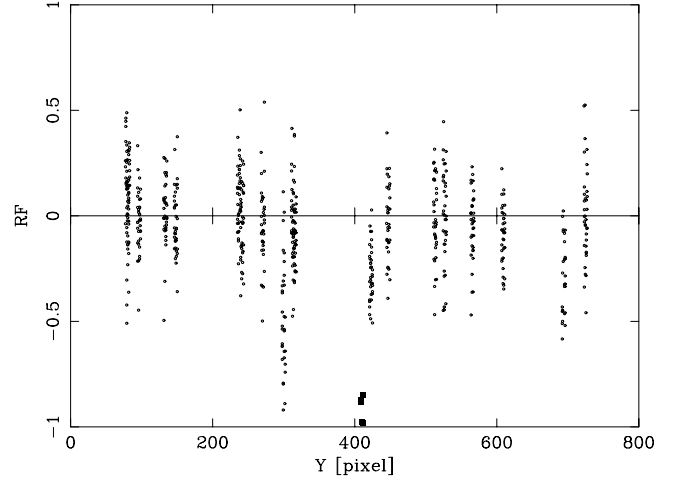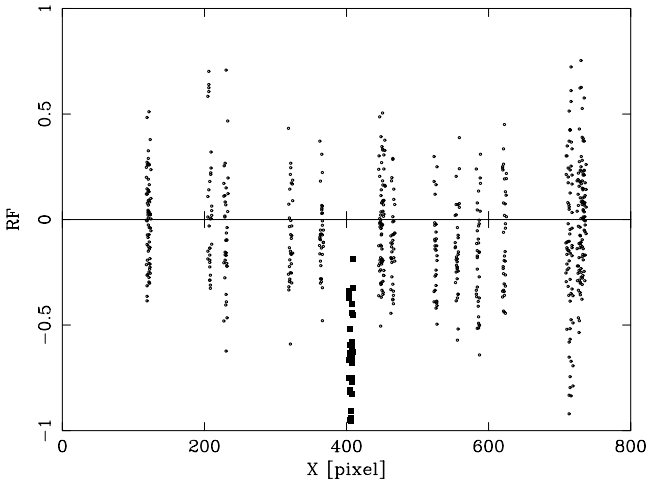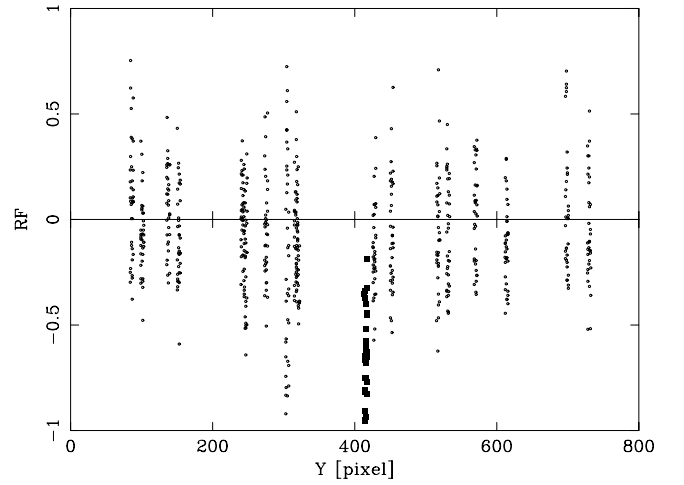
FIG. 5a

FIG. 5b

FIG. 5c

FIG. 5d

FIG. 5e

FIG. 5f

FIG. 5.—Flux residual vs. location for objects in an image of the UMI J1508+6717 field. The plots in the top row display points from 40 images, and the plots in the remaining rows display points from 36 images. The left panels plot $\mathcal{RF}$ vs. the X-coordinate, and the right panels plot $\mathcal{RF}$ vs. the Y-coordinate. The filled squares represent the QSO. Panels a and b correspond to the 1999 epoch, c and d to the 2001 epoch, and e and f to the 2003 epoch. For ease of comparison, all the plots have the same scale on the vertical axis.

102
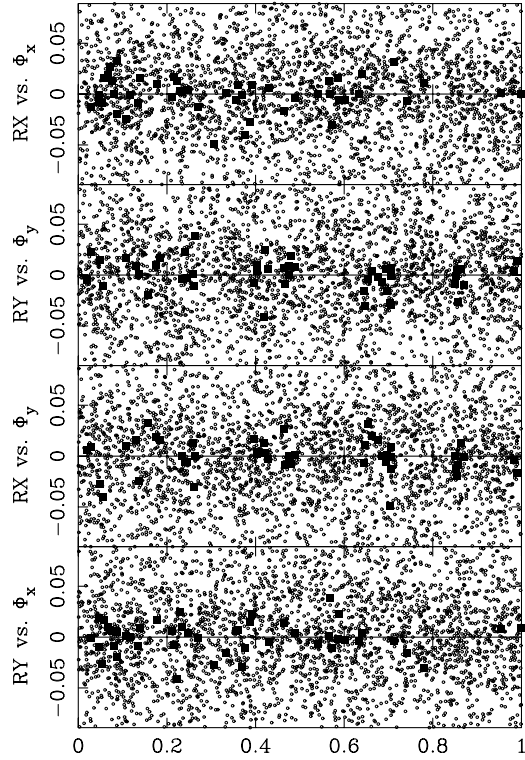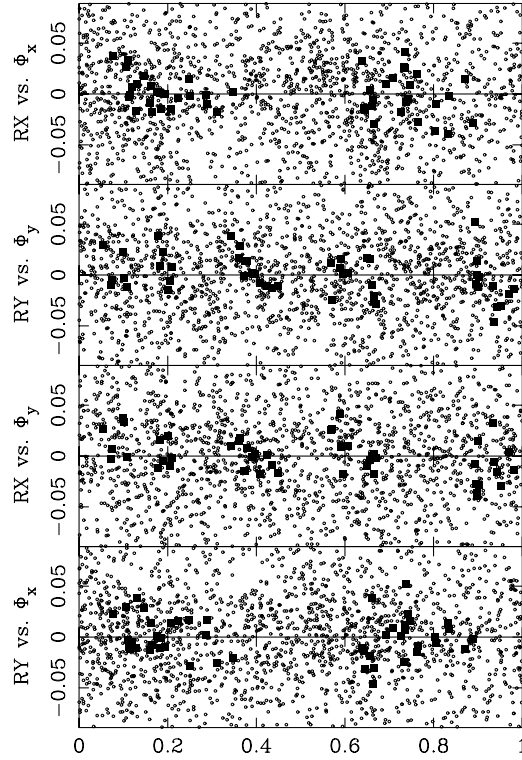
Fig. 6a

Fig. 6b

Fig. 6c

Fig. 6.—Position residuals of the UMI J1508+6716 field, $\mathcal{RX}$ and $\mathcal{RY}$, as functions of the pixel phase, Φ_x and Φ_y. The panels *a*, *b*, and *c* correspond to the epochs 2000, 2001, and 2002, respectively. The filled squares correspond to the QSO.
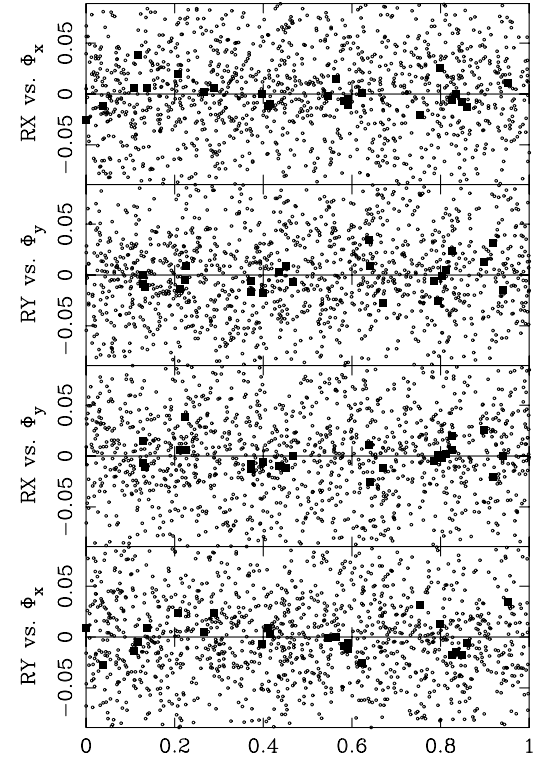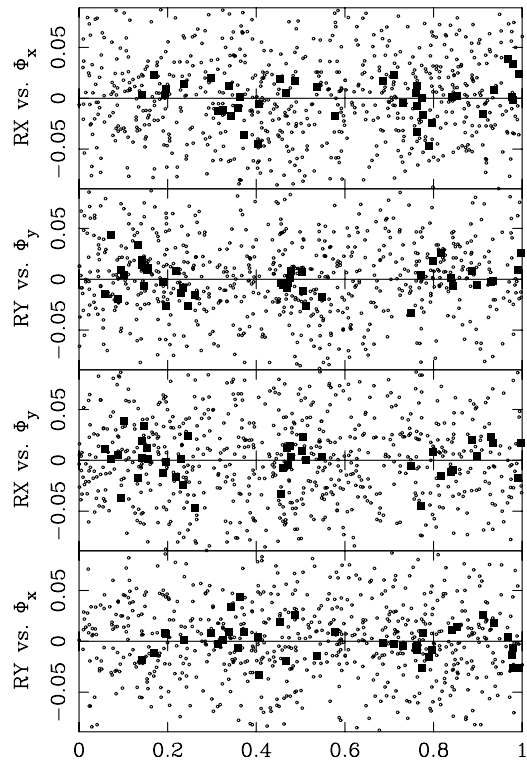
FIG. 7*a*
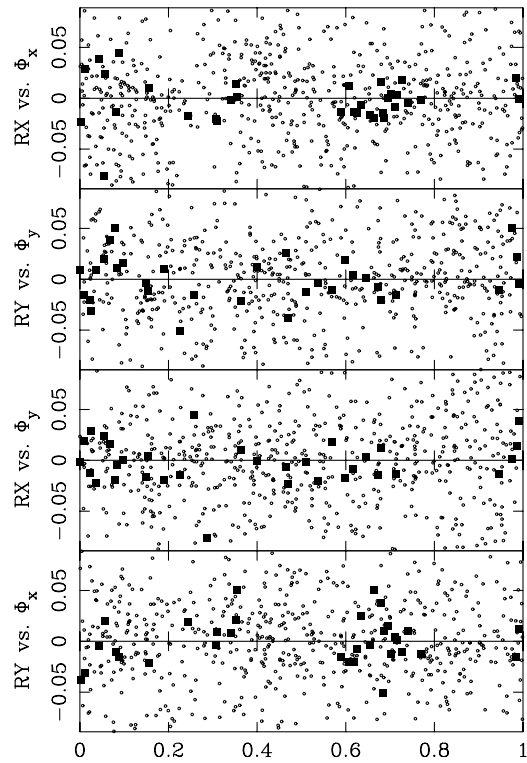
FIG. 7*b*
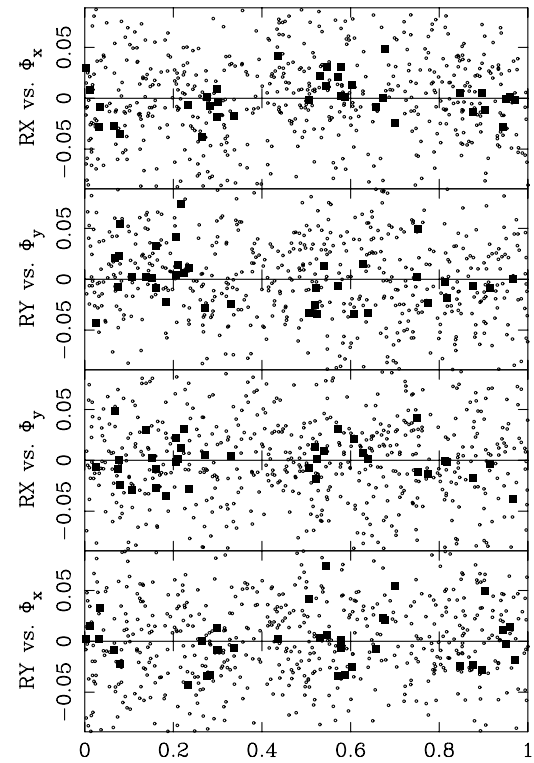
FIG. 7*c*

FIG. 7.—Position residuals of the UMI J1508+6717 field, $\mathcal{RX}$ and $\mathcal{RY}$, as functions of the pixel phase, Φ_x and Φ_y. The panels *a*, *b*, and *c* correspond to the epochs 1999, 2001, and 2003, respectively. The filled squares correspond to the QSO.

FIG. 8a

FIG. 8b

FIG. 8c

FIG. 8.—The rms scatter around the mean of the *X*-component (*top panels*) and the *Y*-component (*bottom panels*) of the centroid as a function of $(S/N)^{-1}$ for the UMI J1508+6716 field. The filled squares correspond to the QSO. The panels *a*, *b*, and *c* correspond to the epochs 2000, 2001, and 2002, respectively.
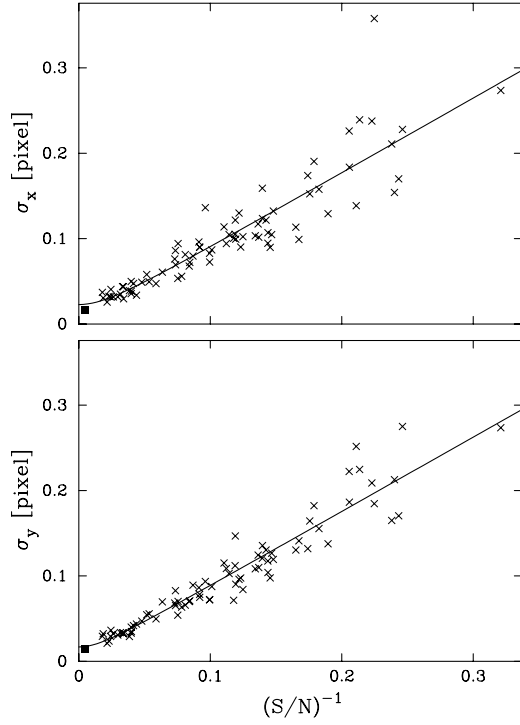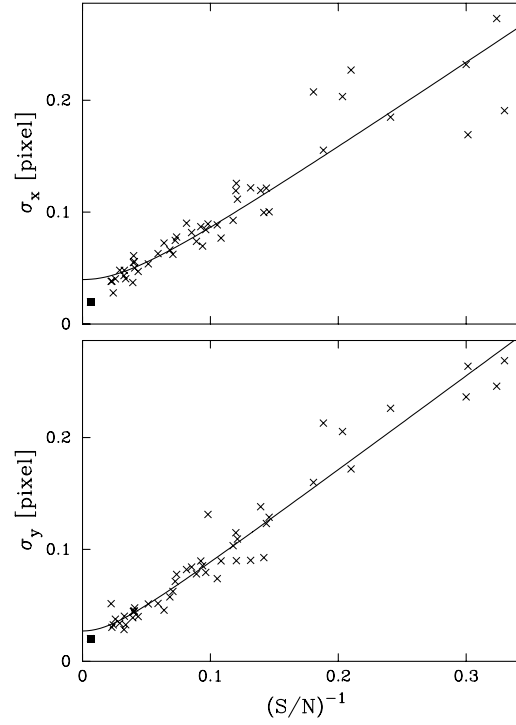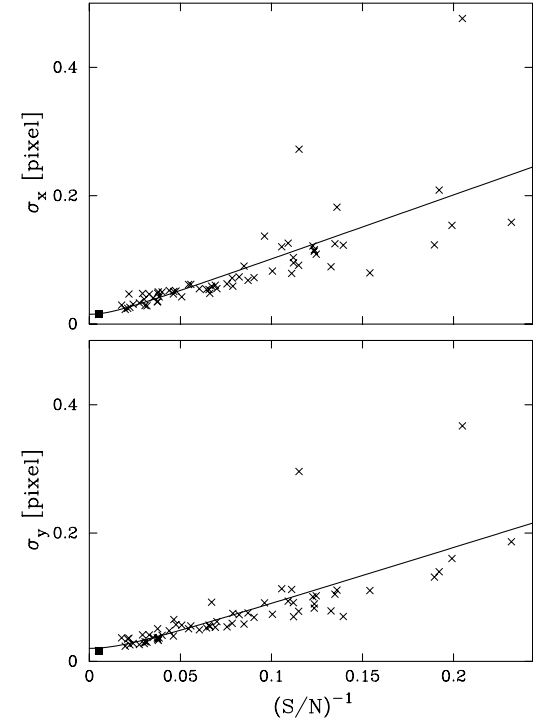
TABLE 1
FITTED FREE PARAMETERS

		X		Y	
		a	σ_0	a	σ_0
FIELD	EPOCH	(pixels)	(pixels)	(pixels)	(pixels)
UMI J1508+6716	2000	0.879	0.023	0.874	0.017
	2001	0.768	0.040	0.846	0.027
	2002	1.004	0.015	0.882	0.020
UMI J1508+6717	1999	0.921	0.024	0.881	0.020
	2001	0.974	0.021	0.926	0.024
	2003	0.987	0.025	0.878	0.030

dither positions instead of the square root of the number of measurements (see eq. [29] in P02). Additional testing while analyzing data for this article shows that the method of P02 and P03 overestimates the uncertainties in the centroids for those objects with high S/N, while underestimating them for those with low S/N.

The usual estimator for the standard deviation about the mean is biased downward when the sample size is small (S. L. Sclove 2004, private communication).[2] For example, the bias is a factor of 0.89 for a sample size of three. This partly explains why P02 find a smaller rms scatter around the mean for measured centroids at a given dither position compared to the scatter for the centroids at all the dither positions together. A better method to estimate the uncertainty in the final average centroid than that used by P02, including the effects of a lack of independence of measurements at a given dither position, is to use the mean centroid, $\bar{z}_k$, at each dither position k. The uncertainty in either the X- or Y-component of the final centroid is

$$\sigma_z = \left[\frac{1}{N_d} \sum_{k=1}^{N_d} (\bar{z}_k - \langle \bar{z} \rangle)^2 \right]^{1/2}, \tag{2}$$

where N_d is the number of dither positions and $\langle \bar{z} \rangle$ is the mean of the mean centroids at the dither positions. The uncertainty estimated with equation (2) is typically 20%–40% larger than the usual estimate from all the measured centroids for an object with an S/N larger than about 15. This increase is less than the approximately 70% increase implied by the procedure of P02, but the increase extends to a lower S/N. This article uses equation (2) to calculate the uncertainty in the mean centroid of an object at one epoch.

4. THE PROPER MOTION OF URSA MINOR

The procedure for deriving a proper motion in this article is different from that described in P02 and P03. Section 4.1 below describes this new procedure in detail for the three-epoch data taken either with STIS or WFPC2. The subsequent sections describe the actual realization of this procedure for the case of Ursa Minor.

4.1. Deriving the Motion of the QSO in the Standard Coordinate System

The three elements needed to determine the relative motion of the QSO with respect to the stars of the dSph are the following: (1) A transformation between the fiducial coordinate systems of the later epochs and that of the first epoch—the "standard coordinate system"—determined by objects com-

mon to all three epochs. The transformation contains a translation, $(\delta x_{j1}, \delta y_{j1})$, a rotation, θ_{j1}, and a ratio between the two scales, s_{j1}. Here j is the index denoting the epoch and, for a transformation, can be 2 or 3. (2) A mean position for an object i, $(\bar{x}^i, \bar{y}^i)$, which is the average of the three measured centroids in the standard coordinate system. The transformed standard coordinates at epochs 2 and 3 are related to the mean coordinate by $(x_j'^i, y_j'^i) = (\bar{x}^i, \bar{y}^i) + (\mu_x^i, \mu_y^i)t(j)$ for the QSO and for any object with a large χ^2 for the scatter around $(\bar{x}^i, \bar{y}^i)$ with $(\mu_x^i, \mu_y^i) = (0, 0)$. Here (μ_x^i, μ_y^i) is the uniform linear motion of the object in the standard coordinate system in pixels yr^{-1}, and $t(j)$ is the time of the epoch j measured from $t(1) \equiv 0$. (3) A simultaneous fit for the coefficients of the transformations, the $(\bar{x}^i, \bar{y}^i)$, and the (μ_x^i, μ_y^i) using all the measured centroids of objects common to the three epochs. Simultaneously fitting for the (μ_x^i, μ_y^i) ensures that the stars of the dSph remain at rest in the standard coordinate system.

Let $(x_j^i \pm \sigma_{xj}^i, y_j^i \pm \sigma_{yj}^i)$ be the measured coordinates and their uncertainties of the centroid of object i in the fiducial coordinate system of epoch j, where $j = 1, 2,$ or 3. The transformation of these measured coordinates to the standard coordinate system is

$$x_j'^i = x_{\text{off}} + \delta x_{j1} + s_{j1} \left[\left(x_j^i - x_{\text{off}} \right) \cos \theta_{j1} - \left(y_j^{*i} - y_{\text{off}} \right) \sin \theta_{j1} \right], \tag{3}$$

$$y_j'^i = y_{\text{off}} + \delta y_{j1} + s_{j1} \left[\left(x_j^i - x_{\text{off}} \right) \sin \theta_{j1} + \left(y_j^{*i} - y_{\text{off}} \right) \cos \theta_{j1} \right], \tag{4}$$

$$\sigma_{xj}'^i = s_{j1} \sqrt{ \left(\sigma_{xj}^i \right)^2 \cos^2 \theta_{j1} + \left(\sigma_{yj}^i \right)^2 \sin^2 \theta_{j1} }, \tag{5}$$

$$\sigma_{yj}'^i = s_{j1} \sqrt{ \left(\sigma_{xj}^i \right)^2 \sin^2 \theta_{j1} + \left(\sigma_{yj}^i \right)^2 \cos^2 \theta_{j1} }. \tag{6}$$

The offset $(x_{\text{off}}, y_{\text{off}})$ defines the pivot point for the rotation: it is pixel (512, 512) for STIS and pixel (400, 400) for WFPC2. The Y-coordinate in equations (3) and (4), y_j^{*i}, includes a correction for the shift caused by the charge traps in the CCD. As discussed at the end of § 2, the equations

$$y_j^{*i} = y_j^i + b \frac{t(j)}{t(3)} \left(1024 - y_j^i \right), \tag{7}$$

$$y_j^{*i} = y_j^i + b \frac{t(j)}{t(3)} y_j^i \tag{8}$$

approximately correct for the shift in the y-direction induced by the charge traps. Equation (7) is for the data taken with STIS, whereas equation (8) is for those taken with WFPC2. These equations are necessary only when the method of Bristow & Alexov (2002) has not been used to restore the images. Because charge traps affect a faint object more than a bright object, an object contributes to the determination of the fitted parameter b, and has its coordinates subsequently corrected, only if its S/N is smaller than some specified limit.

For the three-epoch data, equations (3)–(6) and (7) or (8) contain nine fitted parameters. Their values result from minimizing a χ^2 of the form

$$\chi^2 = \sum_{j=1}^{3} \sum_{i=1}^{N} \left(\left\{ \frac{x_j^i - \left[\bar{x}^i + \mu_x^i t(j) \right]}{\sigma_{xj}'^i} \right\}^2 + \left\{ \frac{y_j^i - \left[\bar{y}^i + \mu_y^i t(j) \right]}{\sigma_{yj}'^i} \right\}^2 \right). \tag{9}$$
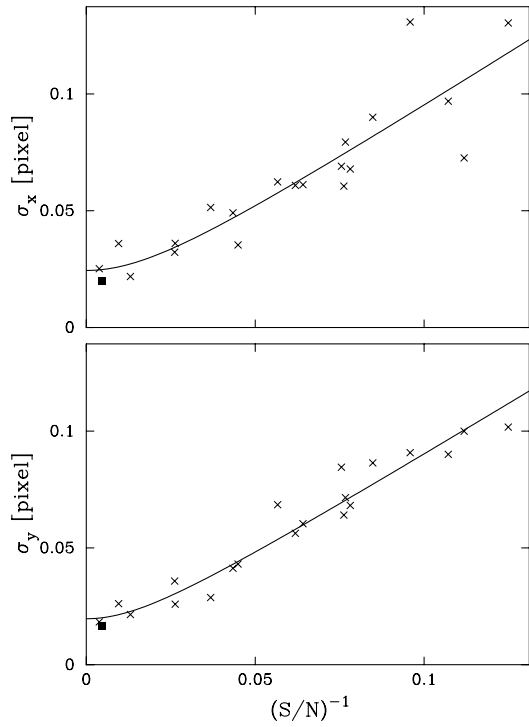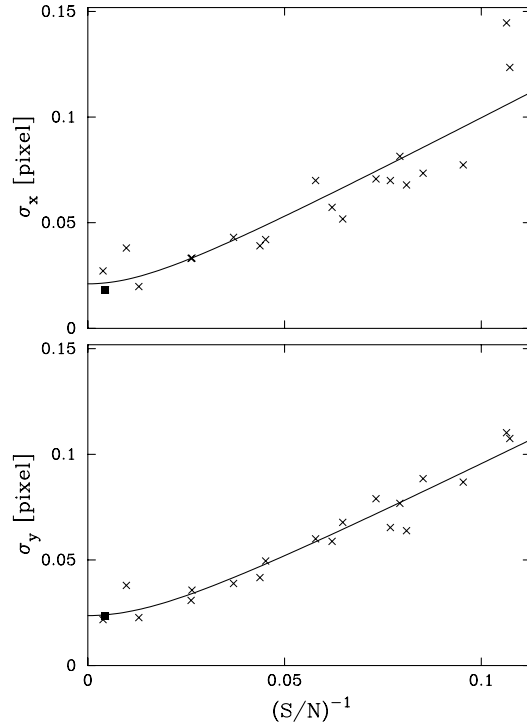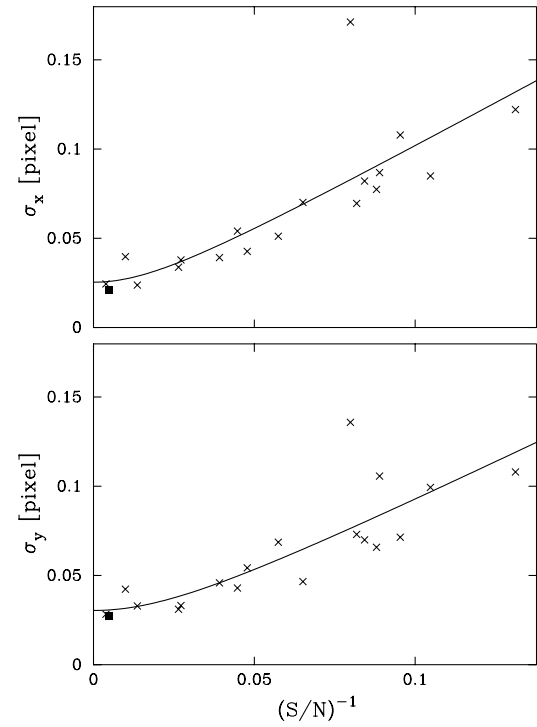
FIG. 9*a*

FIG. 9*b*

FIG. 9*c*

FIG. 9.—Same as Fig. 8 but for the UMI J1508+6717 field. The panels *a*, *b*, and *c* correspond to the epochs 1999, 2001, and 2003, respectively.

The $(\bar{x}^i, \bar{y}^i)$ in the above equations add an additional $2N$ fitted parameters, where N is the number of objects in the fit. However, the $(\bar{x}^i, \bar{y}^i)$ can be calculated analytically. The minimization procedure starts by fitting for the (μ_x^i, μ_y^i) of the QSO while assigning $(\mu_x^i, \mu_y^i) = (0, 0)$ pixels yr^{-1} for all the other objects. The procedure then iteratively selects the object with the largest contribution to the χ^2 and fits for its (μ_x^i, μ_y^i) together with all the previously fitted parameters. The iteration terminates when the highest χ^2 among the objects not yet selected is smaller than some specified limit. The proper motion of a dSph derives from $(-\mu_x, -\mu_y)$ for the QSO.

The uncertainty in (μ_x, μ_y) for the QSO and thus the uncertainty in the proper motion of the dSph comes from increasing the χ^2 by 1 above the minimum (e.g., Press et al. 1992, p. 650). One component of the motion changes away from its fitted value, with all other parameters adjusted to minimize χ^2, until the total χ^2 increases by 1. The difference between this value and the nominal value is the uncertainty for this component of the motion. The procedure repeats for the other component of the uncertainty. A correct determination of the uncertainty in (μ_x, μ_y) using this method requires that the uncertainties in (x_j^i, y_j^i) be realistic. A breakdown of this assumption would be indicated by a minimum total χ^2 that is significantly larger than 1 per degree of freedom.

4.2. Motion of the QSO in the UMI J1508+6716 Field

STIS was the imaging detector in the UMI J1508+6716 field at all the epochs. Thus, it was possible to correct the images for the effects induced by the charge traps in the CCD using the method of Bristow & Alexov (2002). Correcting the images eliminated the need to fit for the free parameter b in equation (7).

The number of objects with measured centroids is 81 for the first epoch, 49 for the second, and 64 for the third. Among these, 32 are common to the three epochs. The choice for the individual χ^2 that triggers fitting for uniform linear motion is 15. There are approximately 4 degrees of freedom per object when the motion is not fitted, so this limit should be triggered by chance for only 0.15 objects in a sample of 32. The final fitted transformation and motion of the QSO are not sensitive to the exact value of this limit. The total χ^2 from equation (9) is much larger than 1 per degree of freedom when using the uncertainties estimated with equation (2). Thus, there must be an uncertainty that arises from an error that is the same for all measurements made at a single epoch but changes significantly between epochs. Figure 10 explores whether this uncertainty is additive or multiplicative by plotting the individual contribution of each object to χ^2 versus S/N. From top to bottom, the panels show the contribution to χ^2 for measurements at the first epoch only, second only, third only, and at all the epochs. The plots show that χ^2 is, on average, the same at all values of S/N. Increasing the uncertainties given by equation (9) with an additional additive uncertainty would decrease the χ^2 values only at high S/N, so Figure 10 indicates that the uncertainty given by equation (2) should be multiplied by a constant instead of having a constant added in quadrature. Multiplying the uncertainties by 1.55 produces a χ^2 of 1 per degree of freedom. This choice for the multiplicative factor ensures that the uncertainties in the proper motions calculated as described at the end of § 4.1 reflect the true scatter of the points about the fitted transformation and proper motions. The χ^2 values in Figure 10 are calculated with the increased uncertainty. We can point to no likely source for the additional error operating between epochs.
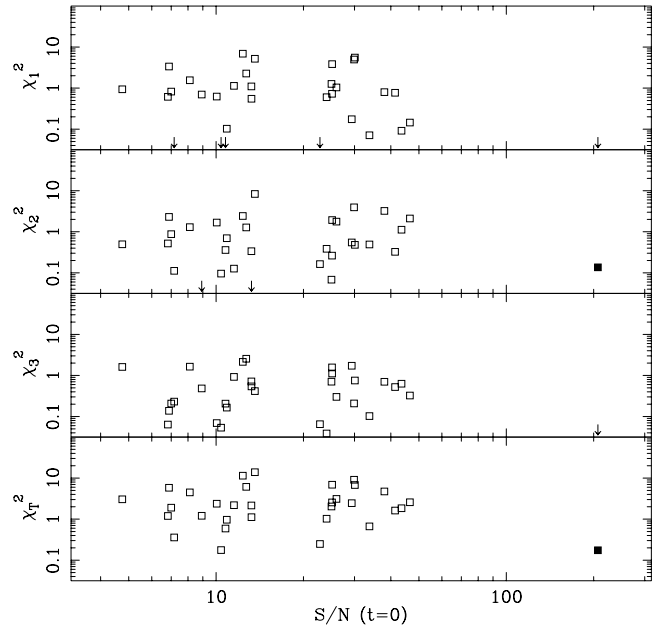

Fig. 10.—χ^2 of an object in the UMI J1508+6716 field, defined by eq. (9), vs. its S/N at the first epoch ($t = 0$). The top three panels show the contributions to the χ^2 from centroids measured at epochs $j = 1, 2$, and 3, respectively, and the bottom panel shows the total χ^2. An arrow pointing down indicates a point outside of the plot range. The filled squares represent the QSO. The gap in the distribution of points between an S/N of about 10 and about 20 is an artifact of the data.

Figure 11 plots position residuals, defined for an object i by

$$RX_{j-1}^i = \bar{x}^i + \mu_x^i t(j) - x_j'^i, \qquad (10)$$

$$RY_{j-1}^i = \bar{y}^i + \mu_y^i t(j) - y_j'^i \qquad (11)$$

as a function of location in the standard coordinate system. Here the subscript $j-1$ indicates that the residual is for a centroid from the jth epoch transformed to the standard coordinate system of the time of the first epoch. From top to bottom, the panels are for the first, second, and third epoch, respectively. The panels in the left column show RX versus X, and those in the right column show RY versus Y. In all the plots, the points scatter around the horizontal axis; no plot shows a trend between RX and X or RY and Y, or a systematic bias toward either positive or negative residuals. The scatter is a few hundredths of a pixel. Although not shown in the figure, the plots of RX versus Y and of RY versus X do not show any trends either.

Figure 12 shows the location of the QSO as a function of time in the standard coordinate system. The top panel shows the variation of the X-coordinate, and the bottom panel does the same for the Y-coordinate. The motion of the QSO is $(\mu_x, \mu_y) = (0.0137 \pm 0.0044, -0.0008 \pm 0.0042)$ pixels yr^{-1}. The contribution to the total χ^2 from the QSO is 0.17, which is reflected in the close agreement between the points and the straight lines in Figure 12. The contribution to the χ^2 has approximately 2 degrees of freedom, which implies an 8% probability of a χ^2 smaller than 0.17 by chance.

4.3. Motion of the QSO in the UMI J1508+6717 Field

WFPC2 was the imaging detector for this field. Because no corresponding software exists that restores an image taken with this detector, equation (8) must be used to account for the shifts in the Y-direction caused by the charge traps. The number of
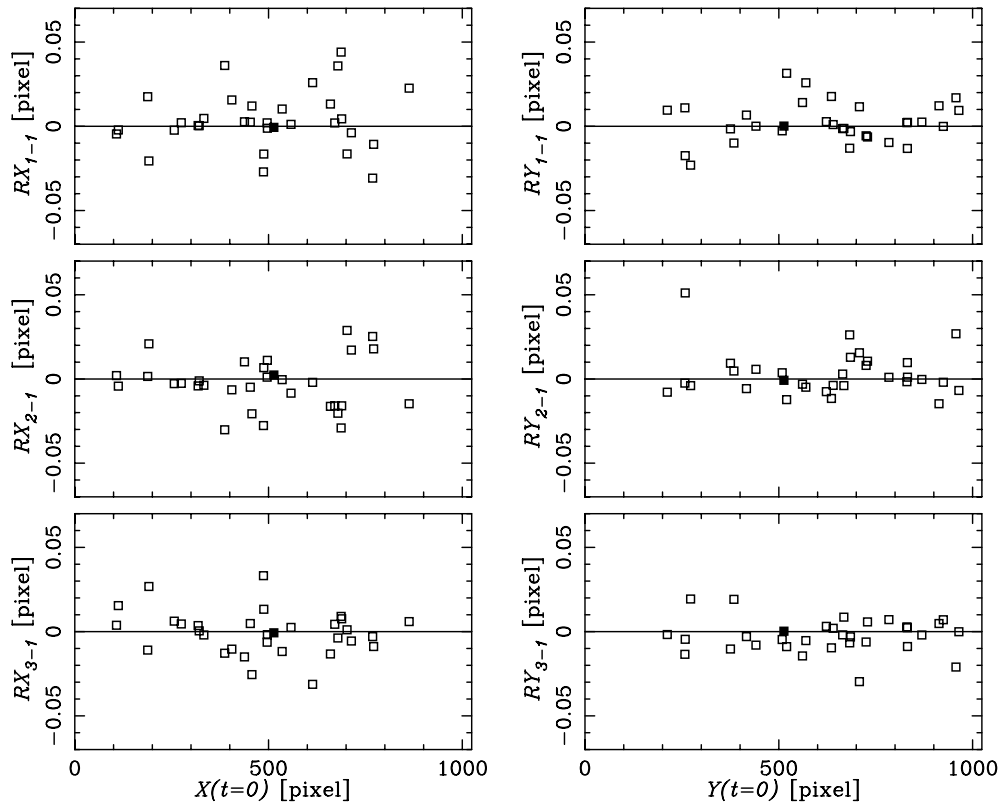
Fig. 11.—Position residuals defined by eqs. (10) and (11) for the objects in the UMI J1508+6716 field. From top to bottom, the panels are for the first, second, and third epoch, respectively. The panels on the left show RX vs. x, and those on the right show RY vs. y. The filled squares correspond to the QSO.

objects with measured centroids is 21 for the 1999 epoch, 20 for 2001, and 19 for 2003. Among these, 19 are common to all the epochs. This is a small number, which proved to be insufficient to precisely determine the value of b in the fitting procedure; the value was large and had the wrong sign. However, b depends on the number of charge traps as a function of time rather than on the observed field. Thus, b was derived from images of a field in Fornax, which contain almost 200 objects and were taken within

Fig. 12.—Location of the QSO as a function of time for the UMI J1508+6716 field in the standard coordinate system. The vertical axis in each plot has the same scale.

a few days of those for UMI J1508+6717. The result is $b = -3.5 \times 10^{-5}$, with the correction applying to objects with S/N < 100. Equation (8) for UMI J1508+6717 has b held constant at this value and applied to objects with S/N < 100. The choice for the individual χ^2 that triggers fitting for uniform motion is 30. This results in fitting a motion for only the QSO and one star with a large motion. We chose not to fit a motion for any other stars because of the small sample size, although the final fitted transformation and motion of the QSO are not sensitive to fitting motions for a few additional objects.

The χ^2 per degree of freedom from equation (9) is again larger than 1 when using the uncertainties from equation (2). Figure 13 plots the contribution to χ^2 versus S/N for objects in UMI J1508+6717. As in Figure 10, the lack of a trend implies that the additional error is multiplicative. A multiplier of 1.413 yields a χ^2 per degree of freedom of 1.

Figure 14 plots the position residuals RX and RY for the UMI J1508+6717 field, similar to Figure 11. No panel shows a trend of RX with X or RY with Y. Although not depicted in the figure, there are no trends between RX and Y or RY and X either.

Figure 15 shows the location of the QSO as a function of time in the standard coordinate system for the UMI J1508+6717 field. Note that the slopes of the corresponding plots in Figures 15 and 12 need not be the same, because the two fields are rotated with respect to each other. The motion of the QSO is $(\mu_x, \mu_y) = (-0.0016 \pm 0.0026, -0.0085 \pm 0.0028)$ pixels yr^{-1}. The contribution to the total χ^2 from the QSO is 0.01, which is reflected in the close agreement between the points and the straight lines in Figure 15. The contribution to the χ^2 has approximately 2 degrees of freedom, which implies a 0.5% probability of a χ^2 smaller than 0.01 by chance.

The small contributions to the χ^2 by the QSO for both the STIS and WFPC2 data suggest that our estimated uncertainties in the
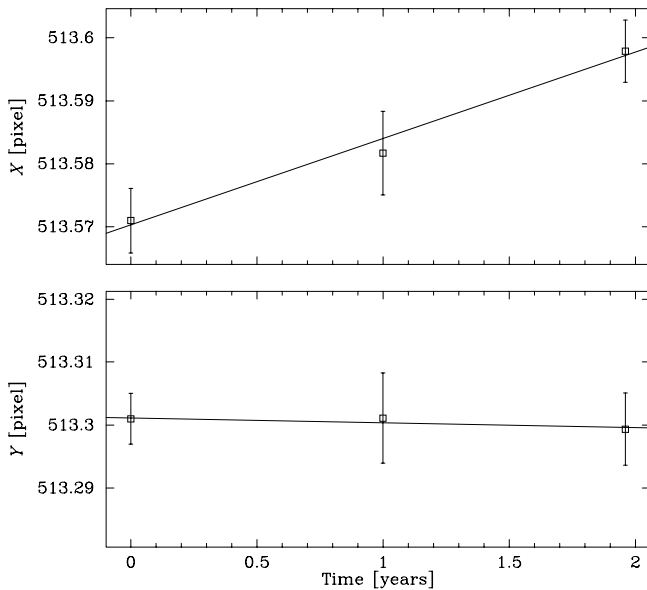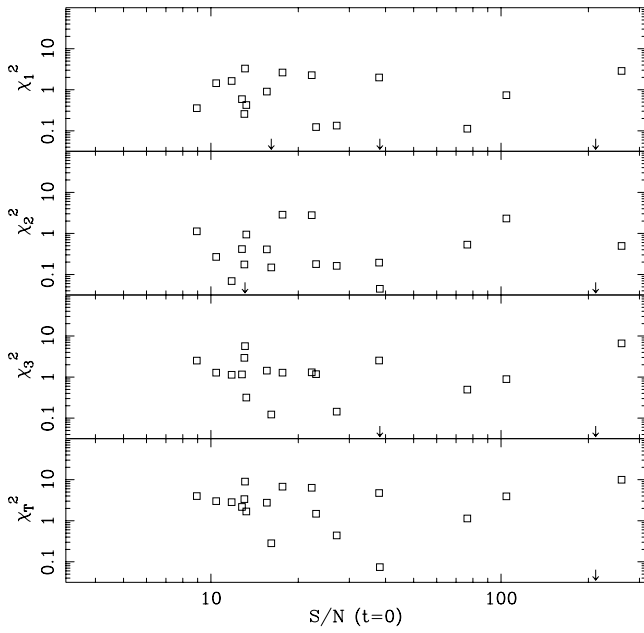
FIG. 13.—Same as Fig. 10 but for the UMI J1508+6717 field. Note that the points corresponding to the QSO are below the lower limit of the plots, as indicated by the arrows at an S/N of 214.

centroids are too small. However, other objects in our fields with fitted motions do not have unusually small χ^2 values (see Tables 2 and 3 presented in § 4.4). A smaller threshold for the contribution to χ^2 that triggers fitting for a motion would reduce the multiplier needed to make the total χ^2 per degree of freedom equal to 1, which would increase the contribution to the χ^2 from the QSO. We choose not to reduce our thresholds further because the small number of stars in both of our fields could produce a systematic

FIG. 15.—Same as Fig. 12 but for the UMI J1508+6717 field.

error in the measured centroids depending on position. The small number both forces us to use an ePSF that is constant in both space and time within an epoch and limits our ability to detect systematic errors. It also limits the amount of information available to determine the transformation to the standard coordinate system. We prefer to average over possible systematic errors rather than spuriously remove them by fitting motions. We then think that it is best to increase the uncertainties in the measured centroids so that the uncertainty in the fitted motion of the QSO reflects the typical scatter of the centroids around the fitted transformation and motions, even if the centroids of the QSO have a smaller scatter. We

FIG. 14.—Same as Fig. 11 but for the UMI J1508+6717 field.

TABLE 2

MEASURED PROPER MOTIONS FOR OBJECTS IN THE UMI J1508+6716 FIELD

ID (1)	X (pixels) (2)	Y (pixels) (3)	S/N (4)	μ_α (mas century^{-1}) (5)	μ_δ (mas century^{-1}) (6)	χ^2 (7)
1..........	514	513	207	0 ± 28	0 ± 27	0.17
2..........	671	640	47	59 ± 35	-140 ± 34	2.58
3..........	321	375	44	-2 ± 39	161 ± 39	1.86
4..........	771	685	38	-1511 ± 48	-1573 ± 46	4.72
5..........	497	831	34	-88 ± 41	-658 ± 41	0.66
6..........	318	665	23	-1027 ± 48	61 ± 48	0.25
7..........	689	623	11	67 ± 69	-216 ± 66	0.96
8..........	453	509	10	-619 ± 94	-649 ± 95	1.27

again emphasize that the measured motion of the QSO does not depend strongly on the sample of objects with fitted motions.

4.4. *Measured Proper Motion*

Table 4 records the measured proper motion for each field in the equatorial coordinate system and their weighted mean. The uncertainty in the proper motion of the dSph depends both on the uncertainty in the measured motion of the QSO in the standard coordinate system and on the length of the time baseline. The baseline for the UMI J1508+6716 field is about 2 yr, whereas that for the UMI J1508+6717 field is about 4 yr. Because of the small number of objects in the latter field, we chose to give the two fields more nearly equal weight in the average. We did this by doubling the uncertainty for the proper motion derived from the UMI J1508+6717 field, and this is the uncertainty listed in Table 4.

The proper motion in Table 4 is that measured by a heliocentric observer and thus includes the effects of the motions of the LSR and of the Sun with respect to the LSR. The measured proper motion is the best quantity to use for comparisons with the other independent measurements.

There are two previous measurements of the proper motion for Ursa Minor. Scholz & Irwin (1993) report a measured proper motion of $(\mu_\alpha, \mu_\delta) = (50 \pm 80, 120 \pm 80)$ mas century^{-1} (the last row in their Table 3 but using the larger uncertainty for μ_δ implied in the text), and Schweitzer (1996; see also Schweitzer et al. 1997) reports a value of $(5.6 \pm 7.8, 7.4 \pm 9.9)$ mas century^{-1}. The four rectangles in Figure 16 depict the four independent measurements of the proper motion. The center of a rectangle is the best estimate of the proper motion, and the sides are offset from the center by 1 σ uncertainties. Rectangles 1 and 2 represent the measurements by Scholz & Irwin (1993) and Schweitzer (1996), respectively, whereas rectangles 3 and 4 represent the measurements from this study for the fields UMI J1508+6716 and UMI J1508+6717, respectively.

Our measurements 3 and 4 agree within their uncertainties. The μ_α components of measurements 2 and 3 disagree, and at least one of these two measurements must be affected by systematic errors larger than the quoted uncertainties. Our other

TABLE 3

MEASURED PROPER MOTIONS FOR OBJECTS IN THE UMI J1508+6717 FIELD

ID (1)	X (pixels) (2)	Y (pixels) (3)	S/N (4)	μ_α (mas century^{-1}) (5)	μ_δ (mas century^{-1}) (6)	χ^2 (7)
1..........	414	414	212	0 ± 21	0 ± 20	0.00
2..........	563	426	77	-166 ± 23	-441 ± 20	2.46

TABLE 4

MEASURED PROPER MOTION OF URSA MINOR

Field	μ_α (mas century^{-1})	μ_δ (mas century^{-1})
UMI J1508+6716	-57 ± 22	41 ± 22
UMI J1508+6717	-40 ± 25	0 ± 24
Weighted Mean	-50 ± 17	22 ± 16

measurement, 4, is closer to 3 than to 2. Because of its large uncertainty, measurement 1 does not provide much additional information on the proper motion. The weighted mean of our measurements 3 and 4, listed in the bottom line of Table 4, differs from measurement 2 by 3.0 times the uncertainty in the difference of μ_α and 0.8 times the uncertainty in the difference of μ_δ. Thus, these two reported measurements do not agree within their uncertainties, and one or the other or both must have systematic errors larger than the quoted uncertainties. Through experimentation, we have eliminated the following sources for the disagreement: (1) The exact shape of the ePSF. Using an analytic ePSF and one derived from archival data sets for a field in the globular cluster ω Centauri had little effect on the final proper motion. (2) The value for parameter b in equation (8), which approximately corrects for the effect of the increasing number of charge traps in the PC CCD. Large and arbitrary changes in the value cannot simultaneously reconcile measurements 2, 3, and 4. (3) Changes in the number of stars that determine the transformation between epochs. The fitted parameters, including the motion of the QSO, do not change significantly if objects with apparently discrepant measurements, i.e., having a large χ^2 after being fitted for a uniform motion, are excluded from the sample. (4) The exact value of the limit on χ^2 that triggers fitting for a uniform motion. Thus, we are unable to explain the origin of the difference between our measured proper motion and that of Schweitzer (1996; see also Schweitzer et al. 1997).
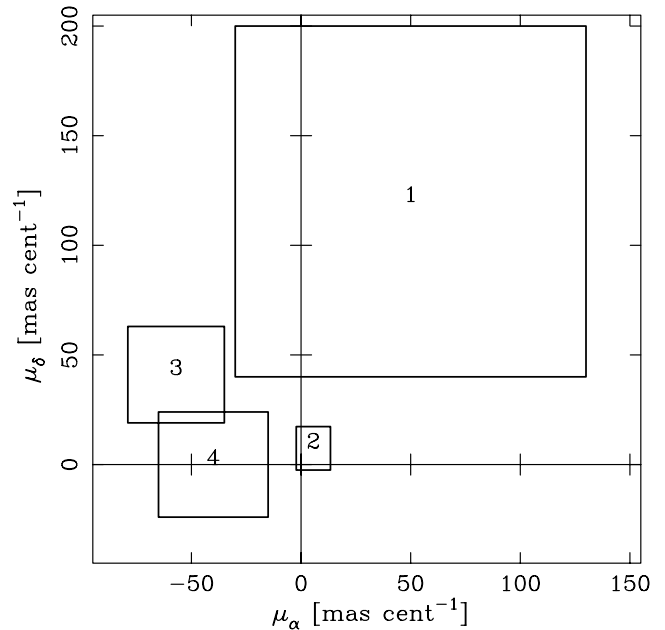

FIG. 16.—Comparison of four independent measurements of the proper motion of Ursa Minor. The center of each rectangle is the best estimate of the proper motion, and the sides are offset by 1 σ uncertainties. Rectangles 1, 2, 3, and 4 correspond to the measurements by Scholz & Irwin (1993), Schweitzer (1996), this study (field UMI J1508+6716), and this study (UMI J1508+6717).

TABLE 5
Galactic Rest Frame Proper Motion and Space Velocity of Ursa Minor

Field (1)	μ_α^{Grf} (2)	μ_δ^{Grf} (3)	μ_l^{Grf} (4)	μ_b^{Grf} (5)	Π (km s^{-1}) (6)	Θ (km s^{-1}) (7)	Z (km s^{-1}) (8)	V_r (km s^{-1}) (9)	V_t (km s^{-1}) (10)
UMI J1508+6716..........................	-15 ± 22	56 ± 22	50 ± 22	-29 ± 22	36 ± 61	-176 ± 74	-138 ± 56	-68 ± 58	216 ± 69
UMI J1508+6717..........................	2 ± 25	16 ± 24	9 ± 25	-13 ± 25	-26 ± 69	-38 ± 84	-96 ± 63	-85 ± 66	64 ± 73
Weighted Mean	-8 ± 17	38 ± 16	32 ± 17	-22 ± 17	9 ± 46	-116 ± 56	-119 ± 42	-75 ± 44	144 ± 50

Note.—Proper motions are in mas century^{-1}.

Table 2 tabulates the proper motions for those objects in the UMI J1508+6716 field for which they were measured. Table 3 does the same for the UMI J1508+6717 field. The first line of each table corresponds to the QSO, and subsequent objects are listed in order of decreasing S/N. The ID number of an object is in column (1), the X- and Y-coordinates of an object in the earliest image of the first epoch (o5bl01010 for UMI J1508+6716 and u50j0101r for UMI J1508+6717) are in columns (2) and (3), and the S/N of the object at the first epoch is in column (4). The components of the measured proper motion, expressed in the equatorial coordinate system, are in columns (5) and (6). Each value is the measured proper motion in the standard coordinate system corrected by adding the weighted mean proper motion of Ursa Minor given in the bottom line of Table 4. To indicate that this correction has been made, the proper motion of the QSO is given as zero. The listed uncertainty of each proper motion is the uncertainty of the measured proper motion, calculated in the same way as for the QSO, added in quadrature to that of the average proper motion of the dSph. The contribution of the object to the total χ^2 is in column (7). The proper motion is unreliable if this value is much larger than 2.0.

4.5. Galactic Rest Frame Proper Motion

Removing the contributions to the measured proper motion from the motion of the LSR and the peculiar motion of the Sun yields the Galactic rest frame proper motion. This proper motion would be measured by a hypothetical observer at the location of the Sun and at rest with respect to the Galactic center. Columns (2) and (3) in Table 5 list the components of the Galactic rest frame proper motion expressed in the equatorial coordinate system, $(\mu_\alpha^{\text{Grf}}, \mu_\delta^{\text{Grf}})$, for our two fields. The derivation of $(\mu_\alpha^{\text{Grf}}, \mu_\delta^{\text{Grf}})$ assumes 220 km s^{-1} for the circular velocity of the LSR, 8.5 kpc for the distance of the Sun from the Galactic center, and $(u_\odot, v_\odot, w_\odot) = (-10.00 \pm 0.36, 5.25 \pm 0.62, 7.17 \pm 0.38)$ km s^{-1} (Dehnen & Binney 1998) for the peculiar velocity of the Sun, where the components are positive if $u_\odot$ points radially away from the Galactic center, $v_\odot$ is in the direction of rotation of the Galactic disk, and $w_\odot$ points in the direction of the north Galactic pole. For convenience, columns (4) and (5) in Table 5 list the components of the Galactic rest frame proper motion in the Galactic coordinate system, $(\mu_l^{\text{Grf}}, \mu_b^{\text{Grf}})$. Columns (6)–(8) list the components of the space velocity in the cylindrical coordinate system centered on the dSph. The derivation of these assumes a heliocentric distance of 76 kpc to Ursa Minor. The components of the space velocity are positive if Π points radially away from the Galactic rotation axis, Θ is in the direction of rotation of the Galactic disk, and Z points in the direction of the north Galactic pole. Columns (9) and (10) list the radial and tangential components of the space velocity with respect to a hypothetical observer at rest at the Galactic center. Column (9) gives the radial component, which is positive if it

points away from the Galactic center, and column (10) gives the tangential component.

5. ORBIT AND ORBITAL ELEMENTS OF URSA MINOR

Knowing the space velocity of a dSph permits a determination of its orbit for a given form of the Galactic potential. This study adopts a Galactic potential that has a contribution from a disk of the form (Miyamoto & Nagai 1975)

$$\Psi_{\text{disk}} = -\frac{GM_{\text{disk}}}{\sqrt{R^2 + \left(a + \sqrt{Z^2 + b^2}\right)^2}}, \quad (12)$$

from a spheroid of the form (Hernquist 1990)

$$\Psi_{\text{spher}} = -\frac{GM_{\text{spher}}}{R_{\text{GC}} + c}, \quad (13)$$

and from a halo of the form

$$\Psi_{\text{halo}} = v_{\text{halo}}^2 \ln\left(R_{\text{GC}}^2 + d^2\right). \quad (14)$$

In the above equations, R_{GC} is the galactocentric distance, R is the projection of R_{GC} onto the plane of the Galactic disk, and Z is the distance from the plane of the disk. All other quantities in the equations are adjustable parameters, and their values are the same as those adopted by Johnston et al. (1999): $M_{\text{disk}} = 1.0 \times 10^{11} M_\odot$, $M_{\text{spher}} = 3.4 \times 10^{10} M_\odot$, $v_{\text{halo}} = 128$ km s^{-1}, $a = 6.5$ kpc, $b = 0.26$ kpc, $c = 0.7$ kpc, and $d = 12.0$ kpc.

Figure 17 shows the projections of the orbit of Ursa Minor resulting from an integration of the motion in the Galactic potential given by equations (12)–(14). The integration extends for 3 Gyr backward in time and begins at the current location of Ursa Minor with the negative of the space velocity given in the bottom line of Table 5. The filled squares mark the current location of the dSph, the filled stars indicate the center of the Galaxy, and the small open circles mark the points where $Z = 0$ or, in other words, where the orbit crosses the plane of the Galactic disk. The large open circle is for reference: it has a radius of 30 kpc. In the right-handed coordinate system of Figure 17, the current location of the Sun is on the positive X-axis. The figure shows that Ursa Minor is close to apogalacticon and has both a moderately inclined and eccentric orbit.

Table 6 enumerates the elements of the orbit of Ursa Minor. The values of the quantities are in column (3), and their 95% confidence intervals are in column (4). The latter come from 1000 Monte Carlo experiments, where an experiment integrates the orbit using an initial velocity that is chosen randomly from a Gaussian distribution whose mean and standard deviation are
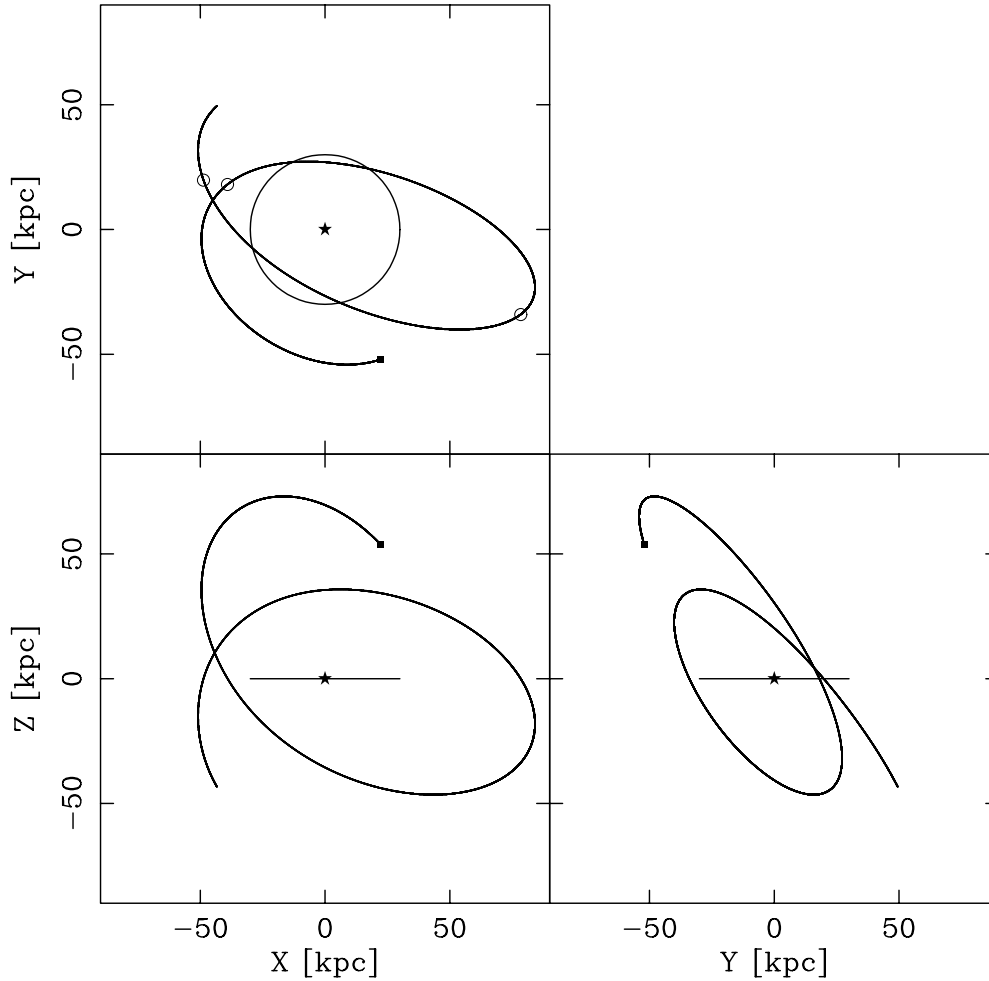
FIG. 17.—Projections of the orbit of Ursa Minor onto the X-Y plane (*top left*), the X-Z plane (*bottom left*), and the Y-Z plane (*bottom right*). The origin of the right-handed coordinate system is at the Galactic center, which is marked with filled stars. The Galactic disk is in the X-Y plane, and the present location of the Sun is on the positive X-axis. The filled squares mark the current location of Ursa Minor at $(X,\ Y,\ Z) = (22,\ -52,\ 54)$ kpc. For reference, the large circle in the X-Y plane has a radius of 30 kpc. The three small circles in the X-Y projection mark the points where Ursa Minor passes through the plane of the Galactic disk. The integration starts from the present and extends backward in time for 3 Gyr.

the best estimate of the space velocity and its quoted uncertainty, respectively. The eccentricity of the orbit, defined as

$$e = \frac{(R_a - R_p)}{(R_a + R_p)}, \qquad (15)$$

is 0.39, although the 95% confidence interval ranges from a nearly circular orbit to a nearly radial orbit with a perigalacticon near 10 kpc. The inclination Φ implies a retrograde orbit. The inclination of the nominal orbit is about $56°$ to the Galactic plane, although a nearly polar orbit is within the 95% confi-

TABLE 6
ORBITAL ELEMENTS OF URSA MINOR

Quantity (1)	Symbol (2)	Value (3)	95% Confidence Interval (4)
Perigalacticon (kpc).........	R_p	40	(10, 76)
Apogalacticon (kpc)	R_a	89	(78, 160)
Eccentricity	e	0.39	(0.09, 0.79)
Period (Gyr)	T	1.5	(1.1, 2.7)
Inclination (deg)..............	Φ	124	(94, 136)
Longitude (deg)	Ω	153	(116, 193)

dence interval. The longitude of the ascending node, Ω, is measured counterclockwise from the positive X-axis.

6. DISCUSSION

6.1. *Is Ursa Minor a Member of a Stream?*

As outlined in § 1, Ursa Minor may be a member of a stream that also includes the LMC, SMC, and the Draco and possibly Sculptor and Carina galaxies. If Ursa Minor is a member, then its predicted measured proper motion is $(\mu_\alpha,\ \mu_\delta) = (-8,\ 13)$ mas century^{-1}, or $|\boldsymbol{\mu}| = (\mu_\alpha^2 + \mu_\delta^2)^{1/2} = 15$ mas century^{-1} with a position angle of $328°$ (Lynden-Bell & Lynden-Bell 1995). The measured proper motion from this study is $|\boldsymbol{\mu}| = 55 \pm 17$ mas century^{-1} with a position angle of $294° \pm 17°$, which are 2.4 σ and 2.0 σ away from the predicted values, respectively. We rule out the possibility that Ursa Minor is a member of the proposed stream at more than 2 σ.

Kroupa et al. (2005) show that the 11 dwarf galaxies nearest to the Milky Way are nearly on a plane, whose pole is at $(l,\ b) = (168°,\ -16°)$. Adopting the direction of the angular momentum vector as the pole of the orbit, the location of the pole is

$$(l,\ b) = (\Omega + 90°,\ \Phi - 90°). \qquad (16)$$

Because of the left-handed nature of the Galactic rotation, prograde orbits have $b < 0$ and retrograde orbits have $b > 0$. Thus, the pole of our orbit for Ursa Minor is $(l, b) = (243° \pm 20°, 34° \pm 11°)$, where the uncertainties are 1 σ values from the Monte Carlo simulations. Thus, the motion of Ursa Minor is not in the plane defined by the nearby dwarf galaxies.

6.2. Star Formation History in Ursa Minor

Studies of the stellar population in Ursa Minor, described in § 1, indicate that the dSph contains low-metallicity, old stars. The majority of stars formed close to a Hubble time ago, suggesting that Ursa Minor lost its gas quickly. In contrast, Carina had extensive star formation about 7 Gyr ago, which continued to within 1 Gyr ago. These two galaxies have nearly the same luminosity and surface brightness and thus presumably should have retained gas to a similar degree. Since they have not, is it because their Galactic orbits are different? The answer appears to be no.

Table 4 of P03 shows that Carina has orbital elements similar to those of Ursa Minor. The perigalacticon of Carina is probably smaller than that of Ursa Minor (a nominal value of 20 instead of 40 kpc), so Carina should have lost its gas more rapidly to stronger tidal shocks (Mayer et al. 2001) and larger ram pressure stripping (Blitz & Robishaw 2000; Gallart et al. 2001; Mayer & Wadsley 2004). A notable difference between the two orbits is that the orbit for Carina is prograde, while that for Ursa Minor is retrograde. However, how this difference could have affected star formation is unclear.

6.3. A Lower Limit for the Mass of the Milky Way

Ursa Minor is bound gravitationally to the Milky Way. The galactocentric space velocity of the dSph imposes a lower limit on the mass of the Milky Way within the present galactocentric radius of the dSph, R. Assuming a spherically symmetric mass distribution and zero for the total energy of the dSph, the lower limit for the mass of the Milky Way is given by

$$M = \frac{R(V_r^2 + V_t^2)}{2G}. \qquad (17)$$

Setting $R = 78$ kpc and using the values from Table 5 for V_r and V_t, $M = (2.4 \pm 1.4) \times 10^{11} \, M_\odot$. This lower limit is consistent with other recent estimates of the mass of the Milky Way, such as the mass of $5.4^{+0.1}_{-0.4} \times 10^{11} \, M_\odot$ within $R = 50$ kpc found by Sakamoto et al. (2003). The Milky Way potential adopted in § 5 has a mass of $7 \times 10^{11} \, M_\odot$ out to $R = 78$ kpc.

6.4. The Effect of the Galactic Tidal Force on the Structure of Ursa Minor

The measured ellipticity of Ursa Minor is one of the largest known for the dSphs. If the Galactic tidal force deformed Ursa Minor from an initial spherical shape to its present elongated shape, then the position angle of its projected major axis should be similar to the position angle of the Galactic rest frame proper motion vector. The position angle of the projected major axis is $53° \pm 5°$, and the position angle of the Galactic rest frame proper motion vector is $348° \pm 25°$. The difference between the two position angles is 2.6 times its uncertainty, arguing that Ursa Minor is not elongated along its orbit.

Gómez-Flechoso & Martínez-Delgado (2003) derive an M/L_V for Ursa Minor in the range of 6–24 by matching the radial profile of a model dSph from N-body simulations to the observed radial profile. In the simulations, the dSph moves on the orbit found by Schweitzer et al. (1997). Given our different orbit for Ursa Minor, is this range of M/L_V values still compatible with the observed limiting radius of the radial profile? A poor man's substitute for numerical simulations is to calculate the tidal radius, r_t, beyond which a star becomes unbound from the dSph. For a logarithmic Galactic potential, r_t is given by (King 1962; Oh et al. 1992)

$$r_t = \left\{ \frac{(1 - e)^2}{[(1 + e)^2/2e] \ln[(1 + e)/(1 - e)] + 1} \frac{M}{M_G} \right\}^{1/3} a. \qquad (18)$$

Here e is the eccentricity of the orbit, a is the semimajor axis $[a \equiv (R_a + R_p)/2]$, M is the mass of the dSph, and M_G is the mass of the Galaxy within a. Equating r_t with the observed limiting radius derived by fitting a King (1966) model, r_k, yields a value for M/L_V for a given orbit. If $r_k = 50'$, then 50% of the orbits in Monte Carlo simulations have $M/L_V > 24$. This M/L_V is just within the range quoted by Gómez-Flechoso & Martínez-Delgado (2003). If $r_k = 78'$, then 50% of the orbits have $M/L_V > 89$, and 95% have $M/L_V > 24$. Thus, the M/L_V derived by Gómez-Flechoso & Martínez-Delgado (2003) is incompatible with the larger measured value of $r_k = 78'$ for our measured proper motion for Ursa Minor. On the other hand, any of the larger values for M/L_V derived from the observed velocity dispersion (see § 1) are more compatible with the larger value of r_k. Equation (18) shows that $M \propto r_t^3$, so the values for M/L derived using this equation are sensitive to the measured value of the limiting radius and the identification of that radius with the tidal radius. Until kinematic measurements definitively identify the tidal radius, an M/L derived with the above argument should be treated with caution.

The average measured M/L_V for Galactic globular clusters is 2.3 (Pryor & Meylan 1993). Could the M/L_V of Ursa Minor be this low? Numerical simulations by Oh et al. (1995) and Piatek & Pryor (1995) show that the ratio of the limiting radius derived by fitting a theoretical King model (King 1966), r_k, to the tidal radius defined by equation (18) is a useful indicator of the importance of the Galactic tidal force on the structure of a dSph. These simulations show that if $r_k/r_t \lesssim 1.0$ the Galactic tidal force has little effect on the structure of the dSph; if $r_k/r_t \approx 2.0$ the effect of the force increases rapidly with increasing r_k/r_t; and if $r_k/r_t \approx 3.0$ the dSph disintegrates in a few orbits. Assuming that $M/L_V = 2.3$ and $r_k = 50'$, $r_k/r_t > 2.0$ for 59% of the orbits generated in Monte Carlo simulations. If $r_k = 78'$ the fraction is 99.6%. Thus, it is unlikely that Ursa Minor would have survived for a Hubble time on its current orbit if it did not contain any dark matter.

7. SUMMARY

1. Two independent measurements of the proper motion for Ursa Minor produce a weighted-average value of $(\mu_\alpha, \mu_\delta) = (-50 \pm 17, 22 \pm 16)$ mas century^{-1} in the equatorial coordinate system for a heliocentric observer. Our value and the proper motion of Schweitzer (1996; also Schweitzer et al. 1997) disagree by more than twice the uncertainty in the difference.

2. Removing the contributions of the motion of the Sun and of the LSR to the measured proper motion gives a Galactic rest frame proper motion of $(\mu_\alpha^{\mathrm{Grf}}, \mu_\delta^{\mathrm{Grf}}) = (-8 \pm 17, 38 \pm 16)$ mas century^{-1} in the equatorial coordinate system for an observer at the location of the Sun but at rest with respect to the Galactic center.

In the Galactic coordinate system, this motion is $(\mu_l^{\mathrm{Grf}},\ \mu_b^{\mathrm{Grf}}) = (32 \pm 17,\ -22 \pm 17)$ mas century^{-1}.

3. For an observer located at the Galactic center and at rest, the radial and tangential components of the space velocity are $V_r = -75 \pm 44$ km s^{-1} and $V_t = 144 \pm 50$ km s^{-1}, respectively.

4. The best estimate for the orbit shows that Ursa Minor is close to its apogalacticon of $R_a = 89$ kpc and is moving closer to the Milky Way on a retrograde orbit with eccentricity $e = 0.39$ and a smallest angle between the orbital plane and the plane of the Galactic disk of $56°$. The closest approach to the Galaxy, perigalacticon, is $R_p = 40$ kpc. Ursa Minor completes one full circuit around the Milky Way in $T = 1.5$ Gyr.

5. Ursa Minor is not a likely member of the "stream" of galaxies on similar orbits proposed by Lynden-Bell & Lynden-Bell (1995), nor is its orbit confined to the plane of satellite galaxies noted by Kroupa et al. (2005).

6. Excluding the possibility of exotic physics, e.g., modified Newtonian dynamics (Milgrom 1983), Ursa Minor must con-tain dark matter to have a high probability of surviving for a Hubble time on its current orbit.

REFERENCES

Aaronson, M. 1983, ApJ, 266, L11
Aaronson, M., & Olszewski, E. W. 1987, in IAU Symp. 117, Dark Matter in the Universe, ed. J. Kormendy & G. R. Knapp (Dordrecht: Reidel), 153
Anderson, J., & King, I. R. 1999, PASP, 111, 1095
———. 2000, PASP, 112, 1360
———. 2003, PASP, 115, 113
Anguita, C., Loyola, P., & Pedreros, M. H. 2000, AJ, 120, 845
Armandroff, T. E., Olszewski, E. W., & Pryor, C. 1995, AJ, 110, 2131
Battinelli, P., & Demers, S. 1999, AJ, 117, 1764
Bellazzini, M., Ferraro, F. R., Origlia, L., Pancino, E., Monaco, L., & Oliva, E. 2002, AJ, 124, 3222
Bennett, C. L., et al. 2003, ApJS, 148, 1
Blitz, L., & Robishaw, T. 2000, ApJ, 541, 675
Bristow, P. 2004, STIS Model-based Charge Transfer Inefficiency Correction Example Science Case 1: Proper Motions of Dwarf Galaxies (CE-STIS-2004-003; Baltimore: STScI)
Bristow, P., & Alexov, A. 2002, Modeling Charge Coupled Device Readout: Simulation Overview and Early Results (CE-STIS-ISR 2002-001; Baltimore: STScI)
Brown, T., et al. 2002, in HST STIS Data Handbook, Ver. 4.0, ed. B. Mobasher (Baltimore: STScI)
Carrera, R., Aparicio, A., Martínez-Delgado, D., & Alonso-García, J. 2002, AJ, 123, 3199
Cudworth, K. M., Olszewski, E. W., & Schommer, R. A. 1986, AJ, 92, 766
Dehnen, W., & Binney, J. J. 1998, MNRAS, 298, 387
Demers, S., Battinelli, P., Irwin, M. J., & Kunkel, W. E. 1995, MNRAS, 274, 491
Eskridge, P. B., & Schweitzer, A. E. 2001, AJ, 122, 3106
Gallagher, J. S., Madsen, G. J., Reynolds, R. J., Grebel, E. K., & Smecker-Hane, T. A. 2003, ApJ, 588, 326
Gallart, C., Martínez-Delgado, D., Gómez-Flechoso, M. A., & Mateo, M. 2001, AJ, 121, 2572
Gómez-Flechoso, M. A., & Martínez-Delgado, D. 2003, ApJ, 586, L123
Gratton, R. G., Fusi Pecci, F., Carretta, E., Clementini, G., Corsi, C. E., & Lattanzi, M. 1997, ApJ, 491, 749
Hargreaves, J. C., Gilmore, G., Irwin, M. J., & Carter D. 1994, MNRAS, 271, 693
Hartwick, F. D. A., & Sargent, W. L. W. 1978, ApJ, 221, 512
Hernquist, L. 1990, ApJ, 356, 359
Heyer, B., et al. 2004, WFPC2 Instrument Handbook, Ver. 9.0 (Baltimore: STScI)
Irwin, M., & Hatzidimitriou, D. 1995, MNRAS, 277, 1354 (IH95)
Johnston, K. V., Sigurdsson, S., & Hernquist, L. 1999, MNRAS, 302, 771
Jones, B. F., Klemola, A. R., & Lin, D. N. G. 1994, AJ, 107, 1333
King, I. R. 1962, AJ, 67, 471
———. 1966, AJ, 71, 64
Klessen, R. S., & Kroupa, P. 1998, ApJ, 498, 143
Kleyna, J. T., Geller, M. J., Kenyon, S. J., Kurtz, M. J., & Thorstensen, J. R. 1998, AJ, 115, 2359
Kleyna, J. T., Wilkinson, M. I., Gilmore, G., & Wyn Evans, N. 2003, ApJ, 588, L21
Kroupa, P. 1997, NewA, 2, 139
Kroupa, P., & Bastian, U. 1997, NewA, 2, 77

Kroupa, P., Theis, C., & Boily, C. M. 2005, A&A, 431, 517
Kuijken, K., & Rich, R. M. 2002, AJ, 124, 2054
Lynden-Bell, D., & Lynden-Bell, R. M. 1995, MNRAS, 275, 429
Martínez-Delgado, D., Alonso-García, J., Aparicio, A., & Gómez-Flechoso, M. A. 2001, ApJ, 549, L63
Mateo, M. 1998, ARA&A, 36, 435
Mayer, L., Governato, F., Colpi, M., Moore, B., Quinn, T., Wadsley, J., Stadel, J., & Lake, G. 2001, ApJ, 559, 754
Mayer, L., & Wadsley, J. 2004, in ASP Conf. Ser. 327, Satellites and Tidal Streams, ed. F. Prada, D. Martínez-Delgado, & T. J. Mahoney (San Francisco: ASP), 230
Mighell, K. J., & Burke, C. J. 1999, AJ, 118, 366
Milgrom, M. 1983, ApJ, 270, 365
Miyamoto, M., & Nagai R. 1975, PASJ, 27, 533
Nemec, J. M., Wehlau, A., & Mendes de Oliveira, C. 1988, AJ, 96, 528
Oh, K. S., Lin, D. N. C., & Aarseth, S. J. 1992, ApJ, 386, 506
———. 1995, ApJ, 442, 142
Olszewski, E. W., & Aaronson, M. 1985, AJ, 90, 2221
Olszewski, E. W., Aaronson, M., & Hill, J. M. 1995, AJ, 110, 2120
Palma, C., Majewski, S. R., Siegel, M. H., Patterson, R., Ostheimer, J., & Link, R. 2003, AJ, 125, 1352
Piatek, S., & Pryor, C. 1995, AJ, 109, 1071
Piatek, S., Pryor, C., Olszewski, E. W., Harris, H. C., Mateo, M., Minniti, D., & Tinney, C. G. 2003, AJ, 126, 2346 (P03)
Piatek, S., et al. 2002, AJ, 124, 3198 (P02)
Press, W. H., Teukolsky, S. A., Vetterling, W. T., & Flannery, B. P. 1992, Numerical Recipes, The Art of Scientific Computing (2nd ed.; Cambridge: Cambridge Univ. Press)
Pryor, C., & Meylan, G. 1993, in ASP Conf. Ser. 50, Structure and Dynamics of Globular Clusters, ed. S. G. Djorgovski & G. Meylan (San Francisco: ASP), 357
Reid, I. N. 1997, AJ, 114, 161
Richstone, D. O., & Tremaine, S. 1986, AJ, 92, 72
Sakamoto, T., Chiba, M., & Beers, T. C. 2003, A&A, 397, 899
Scholz, R. D., & Irwin, M. J. 1993, in IAU Symp. 161, Astronomy from Wide-Field Imaging, ed. H. T. MacGillivray et al. (Dordrecht: Kluwer), 535
Schweitzer, A. E. 1996, Ph.D. thesis, Univ. Wisconsin
Schweitzer, A. E., Cudworth, K. M., & Majewski, S. R. 1997, in ASP Conf. Ser. 127, Proper Motions and Galactic Astronomy, ed. R. M. Humphreys (San Francisco: ASP), 132
Shaklan, S., Sharman, M. C., & Pravdo, S. H. 1995, Appl. Opt., 34, 6672
Stetson, P. B. 1987, PASP, 99, 191
———. 1992, in ASP Conf. Ser. 25, Astronomical Data Analysis Software and Systems I, ed. D. M. Worrall, C. Biemesderfer, & J. Barnes (San Francisco: ASP), 297
———. 1994, PASP, 106, 250
Wilkinson, M. I., Kleyna, J. T., Wyn Evans, N., Gilmore, G. F., Irwin, M. J., & Grebel, E. K. 2004, ApJ, 611, L21
Wilson, A. G. 1955, PASP, 67, 27
Young, L. M. 2000, AJ, 119, 188